

LORETA ANGELA MUSCARELLA
STRAIN EFFECTS ON THE OPTICAL PROPERTIES OF LEAD-
HALIDE PEROVSKITES



Ph.D. Thesis, University of Groningen, October 2021
Loreta Angela Muscarella

Ph.D. Examining committee:

Prof. M.A Loi
Prof. F.C Grozema
Prof. R.A.J Janssen
Prof. M. Tromp
Dr. J.V. Milić

The work described in this thesis was performed between January 2018 and September 2021 at AMOLF, Science Park 104, 1098 XG Amsterdam, The Netherlands and financed by the Netherlands Organization for Scientific Research (NWO).

Printed by IPSKAMP printing

Cover Design by Valerio Favale

Cover Image is a plot of an EBSD measurement of MAPbI₃ film

A digital version of this thesis can be downloaded at amolf.nl

ISSN: 1570-1530



university of
groningen

faculty of science
and engineering

zernike institute for
advanced materials

Strain effects on the optical properties of lead-halide perovskites

PhD thesis

to obtain the degree of PhD at the
University of Groningen
on the authority of the
Rector Magnificus Prof. C. Wijmenga
and in accordance with
the decision by the College of Deans.

This thesis will be defended in public on

18 January 2022 at 09:00 hours

by

Loreta Angela Muscarella

born on 15 January 1994
in Palermo, Italy

Supervisors

Prof. B. Ehrler
Prof. A. Polman

Assessment Committee

Prof. M.A. Loi
Prof. F.C. Grozema
Prof. R.A.J. Janssen

*To Valerio and my family who have always believed in me
And have supported me through these years with love and understanding*

Gutta cavat lapidem non vi, sed saepe cadendo

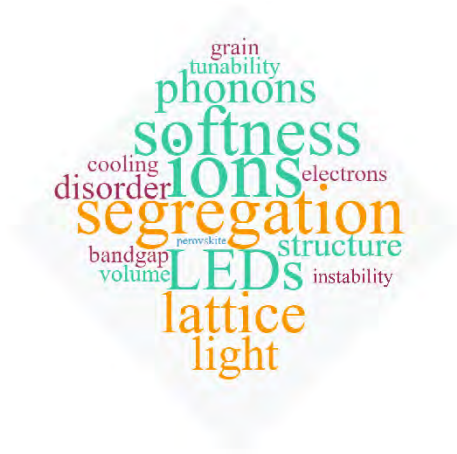
- Lucretius

CONTENTS

1. Introduction & Background	1
1.1. LEAD-HALIDE PEROVSKITES	2
1.2. PROMISES AND CHALLENGES	3
1.3. THE KEY ROLE OF THE LATTICE SOFTNESS	5
1.4. PRESSURE TO MANIPULATE OPTICAL PROPERTIES	6
1.5. ELECTRON BACK-SCATTERED DIFFRACTION	11
1.6. PRESSURE-DEPENDENT SPECTROSCOPY	17
1.7. OUTLINE OF THE THESIS	27
1.8. REFERENCES	30
2. Effects of Grain Size and Orientation on Optical Properties	43
2.1. INTRODUCTION	44
2.2. FABRICATION-DEPENDENT MICROSTRUCTURE	45
2.3. OPTOELECTRONIC PROPERTIES	51
2.4. CONCLUSION	56
2.5. EXPERIMENTAL METHODS	58
2.6. APPENDIX	62
2.6.1. Additional Figures	62
2.6.2. Additional Thickness Travelled by Light	68
2.6.3. Thickness and Roughness Effect on Lifetimes	70
2.6.4. Probing Length in Tr-Microwave Conductivity	72
2.7. REFERENCES	73
3. Pressure Effects on the Hot-Carrier Cooling	81
3.1. INTRODUCTION	82
3.2. PRESSURE-DEPENDENT COOLING	84
3.3. ELECTRON-PHONON CALCULATION	92
3.4. CONCLUSION	95
3.5. EXPERIMENTAL METHODS	96
3.6. APPENDIX	98
3.6.1. Additional Figures	98
3.6.2. Estimation of the Carrier Density	102
3.6.3. Irf Function at 800 nm	103
3.6.4. Maxwell-Boltzmann Fit Function	105
3.7. REFERENCES	106
4. Pressure-dependent Manipulation of Phase Segregation	113
4.1. INTRODUCTION	114
4.2. PRESSURE-DEPENDENT PHASE SEGREGATION	116
4.3. THERMODYNAMICS CHANGES UNDER PRESSURE	123
4.4. KINETICS CHANGES UNDER PRESSURE	129
4.5. CONCLUSION	137
4.6. EXPERIMENTAL METHODS	138
4.7. APPENDIX	141

4.7.1.	Additional Figures	141
4.7.2.	Relation Between the Segregation Rate and the Activation Energy for Halide Migration	149
4.7.3.	Quantification of Halide Migration Using TID	150
4.8.	REFERENCES	153
5.	Pressure Effects on 2D Perovskites	161
5.1.	INTRODUCTION	162
5.2.	PRESSURE-DEPENDENT STRUCTURAL CHANGES	166
5.3.	LOCAL ORIENTATION OF THE ORGANIC SPACER	169
5.4.	PRESSURE-DEPENDENT MECHANOCROMISM	172
5.4.	CONCLUSION	177
5.5.	EXPERIMENTAL METHODS	178
5.6.	APPENDIX	181
5.6.1.	Additional Figures	181
5.6.2.	Additional Tables	187
5.6.3.	Detailed Analysis of Pressure-dependent XRD	195
5.6.4.	Bulk Modulus Calculation	197
5.7.	REFERENCES	199
	Summary	207
	Samenvatting	211
	List of Publications	215
	Acknowledgements	219
	Ringraziamenti	227
	About the Author	235

1. INTRODUCTION & BACKGROUND



In the last 10 years, lead halide perovskites have gathered significant attention for a plethora of applications such as solar cells, LEDs, thermoelectric materials, scintillators and sensors. This class of materials exhibits attractive physical and chemical properties which can be associated with its peculiar electronic and crystal structure. In this Chapter, we first introduce lead halide perovskites, their potential and challenges. We then focus on how the ionic-covalent bond dual nature in these solids is reflected in the mechanically soft and dynamically disordered lattice whose alteration affects the electronic landscape. External pressure can be used as a tool to induce structural modifications of the perovskite lattice and therefore to investigate the structure-properties relationship in these solids. We introduce the main techniques used throughout this thesis: Electron-Backscattered Diffraction (EBSD) to spatially resolve the crystal structure and grain orientation of perovskite thin films; femtosecond pressure-dependent transient absorption and pressure-dependent photoluminescence spectroscopy to correlate the structural variation with optical properties of such films.

1.1. Lead-Halide Perovskites

Perovskites refers to a group of materials with the same crystal structure as calcium titanium oxide (CaTiO_3) described by the formula ABX_3 . Metal-halide perovskites (MHP) feature a monovalent cation such as the organic methylammonium (MA^+ : CH_3NH_3^+), formamidinium (FA^+ : $\text{CH}_2(\text{NH}_2)_2^+$) or the inorganic caesium (Cs^+). B is a divalent cation, usually lead (Pb^{2+}) or tin (Sn^{2+}), and X is the anion, *e.g.*, iodide (I^-), bromide (Br^-) or chloride (Cl^-). A representation of the cubic crystal structure of MHP is shown in **Figure 1.1a**. The crystal structure consists of corner-sharing BX_6 octahedra, with the A cation occupying the 12-fold coordination site in the middle of the cube of eight such octahedra and interacting with the BX_3^- lattice mainly *via* ion-ion, ion-dipole, and hydrogen bonding interactions. The divalent B cation is located at the corner of the cube and surrounded by an octahedron of anions. Deviations from the ABX_3 stoichiometry are also possible when the A and B cations are replaced by a combination of cations having different valences but retaining an overall neutral charge balance (double or quadruple perovskites)^{1,2}.

Incorporation of larger organic cations that do not satisfy the tolerance factor criterium for the formation of the 3D perovskite can result in the formation of low-dimensional layered 2D metal-halide perovskite (LMH)^{3,4}, schematically represented in **Figure 1.1b**. This class of materials consists of infinite 2D slabs of the ABX_3 type structure which are separated by some organic spacers (S). Layered 2D perovskites are often classified into Ruddlesden-Popper (RP) and Dion-Jacobson (DJ) types. The RP perovskites can be described by the formula $\text{S}_2[\text{A}_{(n-1)}\text{B}_n\text{X}_{(3n+1)}]$ ⁵, where the spacer S consists of two monofunctional organic molecules, each of them binding a side of the perovskite slab, whereas van der Waals interactions dominate between the two spacers. In the DJ perovskites, described by the formula $\text{S}[\text{A}_{(n-1)}\text{B}_n\text{X}_{(3n+1)}]$ ⁶, the spacer consists of a bifunctional organic molecule directly binding the two side of the perovskite slab⁷. They are further classified based on the number of perovskite layers (n) which are separated by the organic spacer layer (*e.g.* $n = 1, 2, r$, etc.). In layered 2D perovskites, charges are mostly confined to the inorganic framework as the organic spacers are mostly electronically insulating. This class of materials shows

a unique quantum well behaviour, where for low n , the bandgap decreases as a function of the reduced thickness of the perovskite slab because of the reduced quantum confinement (**Figure 1.1c**). The possibility to choose a larger variety of organic spacers with *ad hoc* functionalities, makes the tunability of the layered 2D perovskites higher in comparison with their 3D counterparts.

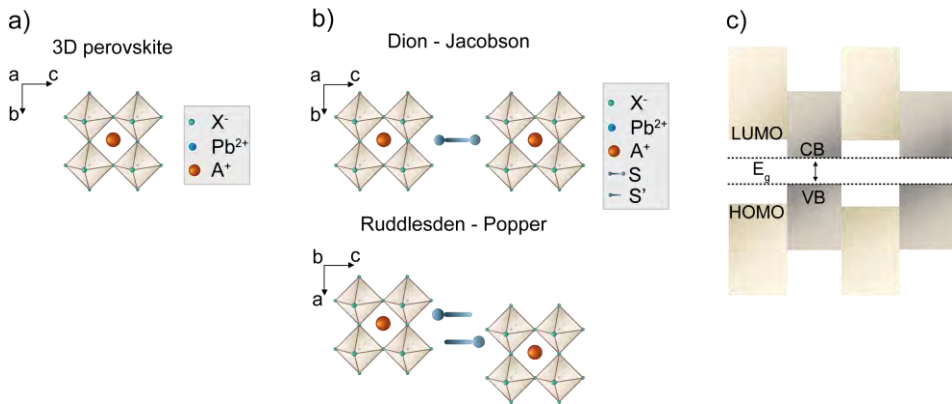


Figure 1.1. From 3D to layered 2D perovskites. A representation of **a**) the crystal structure of 3D MHP, **b**) layered 2D perovskites classified into Ruddlesden-Popper and Dion-Jacobson types, and **c**) their quantum well behaviour, with the energy bandgap (E_g) defined by conduction band (CB) and valence band (VB) edges and the highest occupied molecular orbital (HOMO) and the lowest occupied molecular orbital (LUMO) levels.

1.2. Promises and Challenges

Lead-halide perovskites have recently gathered significant attention due to the high efficiency of perovskite-based solar cells and other optoelectronic devices combined with the possibility for low-cost and simple solution or vapour-based fabrication methods^{8,9}. Their bandgap tunability is one of the most exciting properties for lighting applications, displays and tandem solar cells where the possibility of choosing the bandgap of the material used is quintessential. The simplest and most studied perovskite is the methylammonium lead iodide (MAPbI₃). Any intermediate bandgap between the full iodide MAPbI₃ (1.65 eV)

1 - Introduction & Background

and the full bromide MAPbBr_3 system (2.3 eV) can be obtained^{10,11} by partially replacing the iodide species with bromide. Replacing iodide or bromide with chloride is also possible, opening the possibility to extend the bandgap tunability toward the UV¹². To a minor extent, the bandgap tunability is also achieved by replacing the methylammonium MA^+ cation with a different monovalent A^+ cation with different properties (*e.g.* size¹³, hydrogen bonding donor character¹³). Together with the bandgap tunability, the high photoluminescence quantum efficiency (PLQE) makes perovskites promising for solar cells and light-emitting diodes (LEDs). As a matter of fact, in solar cells the PLQE is directly related to the open-circuit voltage (V_{oc})¹⁴ and is an important metric to optimize the luminous efficiency of LEDs¹⁵. So far, despite the PLQE is reduced by the presence of defects^{14,16–18}, perovskites have demonstrated to be relatively defect tolerant^{19,20} which partially relax the requirements for the fabrication strategies.

Another intriguing property of this class of materials is their low thermal conductivity^{21,22} and the consequent slow heat transport. For instance, the thermal conductivity κ at room temperature of CsPbBr_3 ²³ and MAPbI_3 ²⁴ single crystals is found to be 1 and 0.5 $\text{W m}^{-1} \text{K}^{-1}$, respectively. In contrast, GaAs ²⁵ and silicon²⁶ exhibit a thermal conductivity κ of 52 and 150 $\text{W m}^{-1} \text{K}^{-1}$, respectively. A significant difference in thermal conductivity is also found between rocksalt IV–VI materials (*e.g.* SnTe , $\kappa = 4 \text{ W m}^{-1} \text{K}^{-1}$) and zincblende III–V materials (*e.g.* InSb , $\kappa = 16 \text{ W m}^{-1} \text{K}^{-1}$) and often attributed to their different structural coordination, octahedral and tetrahedral, respectively. Compounds with octahedral coordination often exhibit low thermal conductivity in comparison with other structural coordination (*e.g.* tetrahedral) and this has been attributed to the reduced ability for an atom to vibrate given the larger number of neighbours²⁷. However, vacancies²⁷, the phonon lifetime²⁸ and the phonon mean free path can also affect the overall thermal conductivity. Despite a full picture of what causes the low thermal conductivity in lead-halide perovskites is still missing, the polar nature of these semiconductors together with its structural disorder are key. Differences in thermal conductivity are also present within the class of lead-halide perovskites. Replacing the organic cation (MA^+) with an inorganic one (Cs^+) halves the density of states of accessible modes, resulting in higher thermal conductivity. Furthermore, the lower thermal conductivity of MAPbI_3 is

1.3 - The Key Role of the Lattice Softness

attributed to its particular crystal structure, involving the slow rotation of the MA⁺ cation within the unit cell that changes the cation-lattice coupling^{29,30}. This property opens up applications where slow heat transport is required, such as in thermoelectric devices³¹. Linked to the low thermal conductivity, a slow energy dissipation is also observed on the picosecond timescale. When semiconductors are photoexcited with a photon energy larger than their bandgap, hot carriers are generated (*i.e.*, high-energy electrons in the conduction band and high-energy holes in the valence band). In solar cells, the collection of these electrons (holes) is typically preceded by the loss of the excess of energy until they reach the minimum of the conduction band (maximum of the valence band). This process, known as *hot-carrier cooling*^{32–34}, occurs in the picosecond timescale when all the charges have reached a common temperature and start to interact with the lattice through carrier-phonon scattering to lose the excess of energy. The process is complete when the charges have reached the thermal equilibrium with the lattice. Manipulating this process is critical for many applications, from thermoelectric devices³¹ where slow hot-carrier cooling is preferred to lasers³⁵ where short hot-carrier cooling time is desired for efficient radiative recombination³⁶. These are only a few of the most interesting properties that perovskites exhibit, suggesting their versatility for several applications, not only as active absorber for PV applications.

1.3. The Key Role of the Lattice Softness

The bonding nature within the anionic inorganic framework in lead-halide perovskites exhibit a dual covalent and ionic nature³⁷ and electrostatic interactions dominate between ions with net charge making lead-halide perovskites polar semiconductors³⁸. In addition, H-bonding interactions between the A⁺ cation and the halide in the inorganic framework are present when the A⁺ is organic³⁹. This weaker bond nature compared to the purely covalent bond exhibited by silicon is reflected in the mechanically soft and dynamically disordered perovskite lattice whose alteration affects the electronic landscape of these solids. In addition, this class of materials tends to easily form vacancies and other defects in the lattice^{40–42} that, in combination with the weak ionic bond

1 - Introduction & Background

nature, unlocks the possibility for ions to migrate within the perovskites lattice or, in a solar cell stack, to drift toward the electrode of reverse polarity. This process is called *ion migration*⁴²⁻⁴⁵ and has been identified as one of the main drivers for degradation⁴⁵⁻⁴⁷ affecting the long-term stability of perovskite-based devices. In MAPbI₃, theoretical calculations and experiments show that both the A⁺ cation and the X⁻ anion can migrate with activation energies ranging from 0.46 to 1.12 eV, and 0.08 to 0.58 eV, for MA⁺ and I⁻ respectively⁴⁸⁻⁵¹. The activation energy for the migration of Pb²⁺ is found between 0.80 and 2.31 eV^{48,51}. Thus, due to the high activation energy for the process, Pb²⁺ is unlikely to migrate⁴⁸. Ion migration is observed both in single-halide systems and in mixed-halide systems where the process is more evident under continuous illumination. In mixed-halide perovskites, the halide migration within the perovskite lattice results in a process known as *phase-segregation*⁵²⁻⁵⁴. In this process, halides migrate and form halide-rich domains which in turn affect the bandgap homogeneity (*i.e.* the bandgap of the mixed-halide perovskite is lost and domains of lower and higher bandgap are formed). The lattice softness of lead-halide perovskites also impacts their photodynamics. Several works suggested the formation of polarons (*i.e.* an electron/hole in an ionic crystal together with the induced polarization of the surrounding lattice) after photo-excitation to rationalize the early photophysics and carrier transport dynamics in these materials (*e.g.* slow hot-carrier cooling^{55,56}, low electron-hole recombination rate and long carrier lifetime⁵⁷, defect tolerance⁵⁸, ion migration and phase segregation⁵⁹⁻⁶¹). Thus, a deep understanding of the perovskite lattice and strategies to modify it either by replacing its constitutive elements or by applying external stimuli is key for tuning the optoelectronic properties to access new properties that allow the development of new functional materials.

1.4. Pressure to Manipulate Optical Properties

The impact of the crystal structure on the optoelectronic landscape in perovskites has been discussed in the previous paragraph. Application of external stimuli (*e.g.* temperature, pressure, electric or magnetic field) is a direct way of tuning these properties⁶²⁻⁶⁶. Although temperature has been extensively used as a

1.4 - Pressure to Manipulate Optical Properties

tool for a better fundamental understanding of lead-halide perovskites in combination with several spectroscopic techniques^{43,67-70}, studies related to the pressure-induced effects and thus the structural properties of these materials are still scarce and mainly devoted to the high-pressure range (1-20 GPa)⁷¹⁻⁷⁴. Pressure is a way to externally induce strain in a controlled way, while lattice mismatch during the crystal growth and lattice vibrations within the crystal can also lead to strain within the material. The effect of pressure on the optoelectronic properties of lead-halide perovskites can be understood from the diagram of bonding and antibonding orbitals of a representative APbX₃ that is responsible for the formation of the electronic bandgap as schematically shown in **Figure 1.2** (*left*). The valence band edge is formed by an antibonding combination of halogen *np orbitals* (Cl-3p, Br-4p or I-5p) and Pb *s orbitals* (Pb-6s), and the conduction band edge by an antibonding combination of Pb *p orbitals* (Pb-6p) with negligible coupling with of halogen *p orbitals* (Cl-3p, Br-4p or I-5p)⁷⁵⁻⁷⁷. The lead atomic orbitals contribute to 30-40% of the valence band and 70-90% of the conduction band^{75,78}. Due to the antibonding character of the valence band edge, any change to the perovskite lattice that can increase (decrease) the overlap of the Pb *s orbitals* with the halide *p orbitals* will impact the energy of the valence band edge, moving it towards more positive (negative) potentials. Similarly, the conduction band has an antibonding character. Therefore, any change in the perovskite lattice that can increase (decrease) the overlap of the Pb *p orbitals* with the halide *p orbitals* will impact the energy of the conduction band minimum, moving it towards more positive (negative) potentials.

However, because of the poor coupling of the orbitals forming the conduction band, the changes in the energy level will occur to a minor extent in comparison to the one in the valence band. Although the A⁺ cation does not play a major role in the formation of the electronic bandgap, it induces distortions in the inorganic framework through templating effects and thus plays a critical role in how the Pb and X orbitals overlap, determining many properties of this class of materials. Pressure – and therefore strain – can tune the extent of overlap of Pb orbitals with X orbitals. The main effects of pressure can be related to change in the metal coordination sphere such as bond lengths and interoctahedral tilting⁷⁹ as shown in **Figure 1.2**.

1 - Introduction & Background

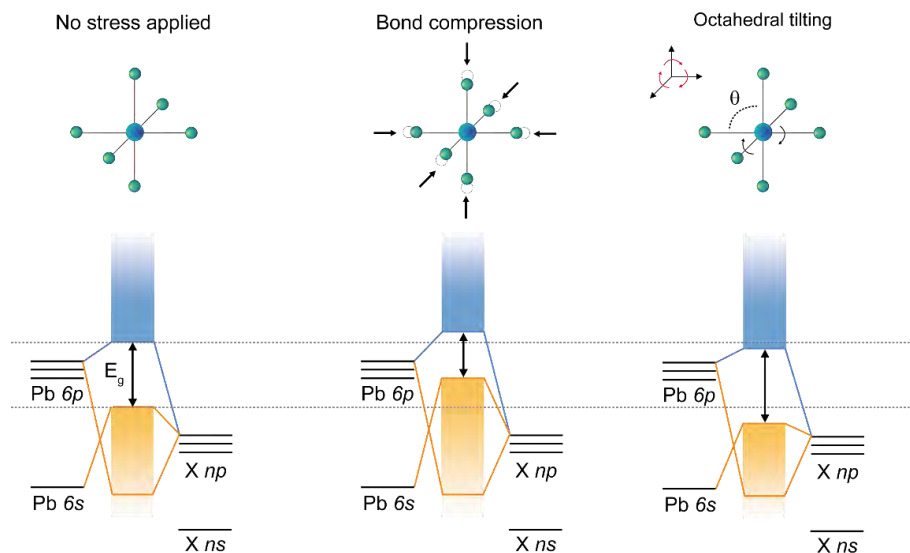


Figure 1.2. External pressure can alter bond length and the octahedral tilting in lead-halide perovskites. On the left, the schematic diagram of bonding and antibonding orbitals of APbX_3 showing the formation of VB and CB with no stress applied. In the middle, the result of external compression when the Pb–X bond length is reduced. The valence and conduction band edge are pushed toward higher energies to a different extent, reducing the bandgap energy. On the right, the band diagram shows the effect of external pressure when altering the octahedral tilting. When the Pb–X–Pb deviates from 180° , the valence band is pushed toward lower energies compared to the conduction band edge resulting in the enlargement of the bandgap energy.

In addition, in the case of layered 2D perovskite, the interlayer spacing distance and lattice packing arrangements are also affected by pressure. Compression of the Pb–X bonds results in higher overlap of the Pb *s* orbitals with the halide *p* orbitals, consequently reducing the bandgap energy. This pressure effect has been observed in many occasions at low pressure (<5 GPa) both in 3D and in layered 2D perovskites^{71,80,81}. Further increasing pressure leads to the contraction of bonds, accompanied by a change in the bond angles which distorts the inorganic

1.4 - Pressure to Manipulate Optical Properties

framework^{82,83}. Depending on the symmetry and orientation of orbitals within the inorganic framework, this can result in enlarged or reduced bandgap due to the change in the overlap between atomic orbitals. In layered 2D perovskites, pressure can affect the distance between inorganic sheets by compressing the organic interlayer spacing and thus enhancing the interlayer electronic interaction. This change leads to a relaxation of the confinement and hence a decrease in bandgap. Depending on the stiffness of the organic molecule^{84–86} used to form the perovskite, pressure can induce a relatively large or small compression of the organic spacer.

On a macroscopic level, the Young's (E) and bulk modulus (K) in Eq. 1.1 and Eq.1.2 can be used as metric to evaluate the material's resistance to axial and uniform compression, respectively. The first is often used for layered 2D perovskites where the unit cell compression has been found to be anisotropic^{81,83} and particularly pronounced along the c -axis, where the organic interlayer spacers sit. K is often used for 3D perovskites and in layered 2D perovskites where the compression is found more isotropic⁸⁰.

The Young's modulus (E) is described by the equation

$$E = \frac{\sigma}{\varepsilon} = \frac{F L_0}{A \Delta L} \quad (1.1)$$

where σ is the uniaxial stress (force F per unit area A) and ε is the axial strain (proportional deformation) in the linear elastic region, L_0 is the original length, ΔL is the change in length (negative under compression, positive when stretched). Soft elastic solids exhibit a low Young's modulus. For example, rubber has a Young's modulus between 0.01 and 0.1 GPa. Contrary, stiff or inelastic solids exhibit high Young's modulus. This is the case for steel that exhibit a Young's modulus between 190 and 215 GPa. Young's modulus always refers to a specific crystal direction and different crystal orientations can exhibit a different Young's modulus.

The bulk modulus (K) is described by the formula

1 - Introduction & Background

$$K = -V \frac{dP}{dV} \quad (1.2)$$

Where V is the final volume after load and $\frac{dP}{dV}$ is the partial derivative of pressure with respect to volume. For comparison, the bulk and Young's moduli of the most common 3D perovskites, layered 2D perovskites with $n = 1$ and conventional semiconductors⁸⁷ are reported in **Table 1.1**.

Table 1.1. Bulk and Young's moduli for the most common conventional semiconductors, 3D and layered 2D lead-halide perovskites ($n = 1$) with butylamine (BA) and phenethylamine (PEA) used as spacers. In brackets is the crystallographic direction to which the Young's modulus is referred.

Material	Bulk Modulus (GPa)	Young's modulus (GPa)
Silicon	105 ⁸⁸	62 <100> ⁸⁹ -188 <111> ⁹⁰
GaAs	75 ⁹¹	84.4 <100> ⁹²
MAPbI ₃	15 ⁹³⁻⁹⁵	10 ⁹⁵ - 14 ⁹⁴ <100>
MAPbBr ₃	24 ⁹³	19.2 <100> ⁹⁶
MAPbCl ₃	45 ⁹⁷	17.7 <100> ⁹⁶
FAPbI ₃	14 ⁹⁸	12.8 <110> ⁹⁶
CsPbBr ₃	22 ⁹⁹	15.6 <101> ⁹⁶
(BA) ₂ PbI ₄	6-8 ¹⁰⁰	8-9 ¹⁰⁰ <001>
(PEA) ₂ PbI ₄	10 ¹⁰¹	11 <001> ¹⁰¹

As can be seen in **Table 1.1**, both the Young's and Bulk moduli of III-V semiconductors and silicon are almost an order of magnitude higher than those of perovskites, confirming the softer nature of the perovskite lattice. Thus, their structure and consequently electronic states tend to be more affected by pressure. There are also larger differences among the perovskite compositions. In the 3D perovskites, when replacing iodine with bromine or chlorine in MAPbX₃ systems, the bulk modulus increases due to the stronger bond between Pb–X which makes the inorganic framework stiffer. In addition, the reduced unit cell volume induced by the replacement of a large halide with a small halide leads to stronger atomic interactions within the perovskite lattice and the overall softness of the material is reduced. The lattice stiffness is also affected by the change in the A⁺ cation. For instance, replacing an organic cation with an inorganic one as caesium (Cs⁺)

results in a stiffer lattice. In the layered 2D perovskites, a key role is played by the organic interlayer spacer. For this class of materials, the mechanical properties are not only related to the inorganic framework but also to the stiffness of the organic molecule used in the composition. The large parameter space of the organic molecules used as spacers allows for designing materials with different flexibility. It is worthwhile to mention that not only the spacer itself delineates the structural-optoelectronic properties relationship but also how the organic spacer packs in the crystal.

So far, studies in a relatively mild range of pressure (< 1 GPa) are rare. This means we are missing important information about the material's behaviour in a strain range that can be introduced during the manufacturing process or during operation (*e.g.* from polaron formation). In addition, these studies can pave the way toward new applications that exploit perovskite's mechanochromic properties expanding the perspective for their future applications¹⁰²⁻¹⁰⁴. No less important is investigating perovskite's properties under mild range of pressure for a deeper understanding of fundamental properties and mechanisms often overlooked when studying materials at high pressures. In turn, understanding of pressure-induced modifications is quintessential for a systematic implementation of this pressure through compositional engineering to permanently realize the effects of mechanical compression.

1.5. Electron Back-Scattered Diffraction

Despite the remarkable properties of halide perovskites due to the softer lattice in comparison with conventional semiconductors such as silicon and III-V semiconductors, the softness of the lattice is also responsible for reduced stability of the perovskites under some experimental conditions. In particular, lead-halide perovskites with an organic A^+ cation exhibit significant instability under electron beam irradiation^{105,106} complicating the study of the microstructure with some of the most common scanning electron microscopy-based (SEM) techniques (*e.g.* cathodoluminescence, electron back-scattered diffraction). Given the profound relation between structural and optoelectronic properties of these materials, sensitive and less destructive techniques are required to probe their

1 - Introduction & Background

microstructure. In metallurgy, geology, and in the ceramics sector, electron-back scattered diffraction (EBSD) is used as a powerful technique to identify the presence of different crystal phases with high spatial resolution, characterise the grain size and the strain among grains, discriminating compounds with similar crystal structures and the temperature response of crystal structures. Combining good spatial resolution, large scale coverage and the simple implementation in SEM-based tools, EBSD is one of the leading techniques for investigation of a material's microstructure^{107,108}. In this paragraph, based on this reference¹⁰⁹, we expand on the working principle of EBSD together with its potential and limitations as a tool to investigate the microstructure of lead-halide perovskites. In addition, we discuss the importance of the image processing and the indexing procedure to extract crystallographic information from the diffraction patterns collected. EBSD is a SEM-based technique where the incident electron beam interacts with a crystalline material and diffracted backscattered electrons are collected forming the so-called Kikuchi patterns. Electrons from the electron beam penetrating in the sample are elastically and inelastically scattered. This results in a diverging source of electrons with a broad range of energies. Those electrons which have undergone elastic and quasi-elastic scatter events and thus lost only a small quantity of energy - in the range of a few eV – can escape from the specimen and if they satisfy Bragg's law they can diffract into cones (Kossel cones) with the cone axis normal to the diffraction plane normal. Then, the Kossel cones intersect with a planar detector (usually a phosphor screen) and the typical nearly straight Kikuchi lines appear. Those lines lie on a diffuse background generated by the inelastically scattered electrons having lower energies. The combination of Kikuchi lines provides a direct measurement of the crystallographic orientations of the specimen. A schematic representation of the technique, working principle and the typical Kikuchi pattern collected are shown in **Figure 1.3**.

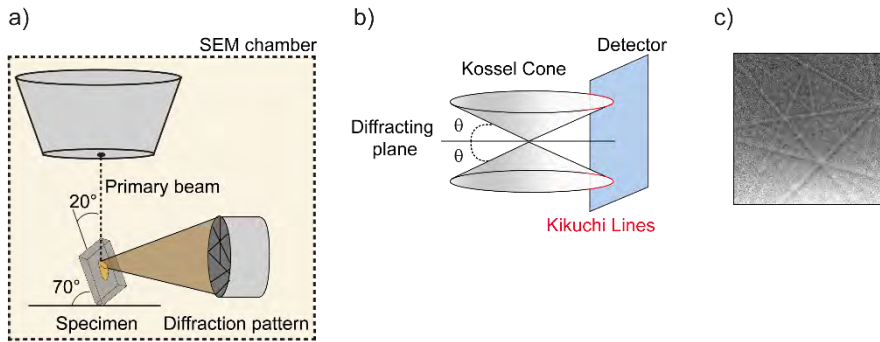


Figure 1.3. EBSD for probing the material's microstructure. **a)** Schematic representation of a typical EBSD setup¹⁰⁹, **b)** Kikuchi lines originating from a diffracting plane at the intersection of the Kossel cone and the detector and **c)** the experimental Kikuchi pattern obtained from MAPbI₃ thin film¹⁰⁹.

The EBSD system used in this thesis has an angular resolution of about 0.5° . The angular resolution of EBSD is related to the quality and sharpness of the diffraction patterns and therefore how well a Kikuchi pattern can be indexed. The depth resolution of the EBSD is limited by the excitation volume which is the interaction volume of the primary electrons within the sample from which electrons are backscattered, forming the typical diffraction patterns.

From a Monte Carlo-based simulation (CASINO¹¹⁰) where 15 keV is used as primary beam voltage, we estimate the 50% escape probability of electrons in the interaction volume to be from 35 nm below the surface for a 70° tilted sample. For a 0° tilted sample these electrons could escape from 260 nm below the surface as shown in **Figure 1.4**. Thus, tilting the sample makes EBSD a more surface sensitive technique. The spatial resolution depends on the sample volume where electrons undergo elastic scattering events. When the electron beam interacts with the tilted specimen, the largest electron density and the largest escape probability are both located close to the spot where the beam enters the sample (grey scale in **Figure 1.4**). The interaction volume is hence close to the beam size. In the example below for electrons with 50% escape probability is about 9 nm at 6 nm beam size, which then defines the lateral resolution.

1 - Introduction & Background

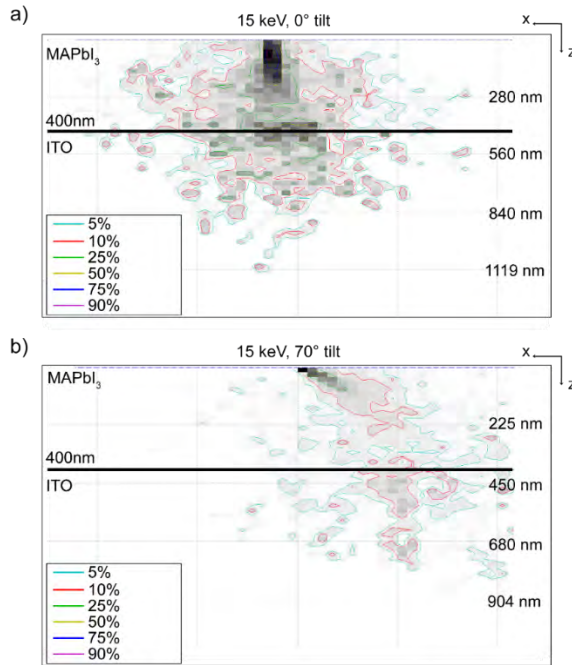


Figure 1.4. Simulated interaction¹⁰⁹ volume between 15keV electron beam and 400nm MAPbI₃ perovskite on ITO obtained using a Monte Carlo simulator (CASINO). **a)** Interaction volume in the X-Z plane of back-scattered electron beam at 0° (no tilt applied) and **b)** 70° tilt (EBSD configuration). The X direction (3 nm/pixel) is parallel to the surface and Z direction corresponds to the thickness of the sample. The percentages shown represent the escape probability of back-scattering electrons from different locations in the sample (e.g. 50% of escape probability represented by the yellow line).

The smallest reasonable step size is the lateral resolution. However, the choice of such small step size is impractical as the total number of collected points would be extremely large and would require many hours of collection with the risk of damaging the material. Using an extreme example, a 500 μm x 500 μm scan area with a 10 nm step size would result in 2.5×10^8 data points. If we consider 2s as typical exposure time per data point in a conventional EBSD system, the measurement will require 158 years. In practice, a step size small enough to resolve the desired features (e.g. grain size) is chosen. During the experiment, the

sample is mounted at 70° with respect to the horizontal to maximize the collection yield of the backscattered electrons, and the detector is placed horizontally on the side a few centimeters away from the specimen as shown in **Figure 1.5**. As mentioned earlier, Kossel cones intersect with a planar detector and the so-called Kikuchi lines emerge from a diffuse background generated by the inelastically scattered electrons forming characteristic Kikuchi patterns. The Kikuchi patterns can be described as a gnomonic projection of the crystal lattice on the flat screen where the angles between the projected planes correspond to the interplanar angles, the band crossings to zone axes of the crystal lattice, and the width of the bands is related to the interplanar spacing, d_{hkl} , as follows from Bragg's law. Kikuchi bands are converted into points by the mathematical Hough's transformation as they are easier to locate and fit automatically. To enhance the Kikuchi lines from the background, we use a Python script to average the background from at least 1000 Kikuchi patterns and divide the pattern from the measurement by this background to correct for spatial differences in collection efficiency. In addition, we apply brightness corrections to remove fluctuations of individual quadrant brightness from frame to frame (usually observed working at low beam current).



Figure 1.5. *Geometry of the EBSD setup used in this thesis¹⁰⁹.* On the left, the direct-electron detector facing the sample mounted on a metallic stub and the sample is tilted by 70° with respect to the horizontal. Above the sample, the source of electrons is shown, operating at a few millimetres distance from the surface of the sample.

1 - Introduction & Background

The result of our image processing is adapted from reference ¹¹¹ and shown in **Figure 1.6**. We index the Kikuchi patterns using OIM Analysis™ from EDAX. The rotation of the probed crystal results in a rotation of the Kikuchi pattern, whereas a tilting of the crystal orientation results in a shift of the pattern. To index the Kikuchi patterns, it is necessary to input the correct crystal structure of the material and an accurate calibration.

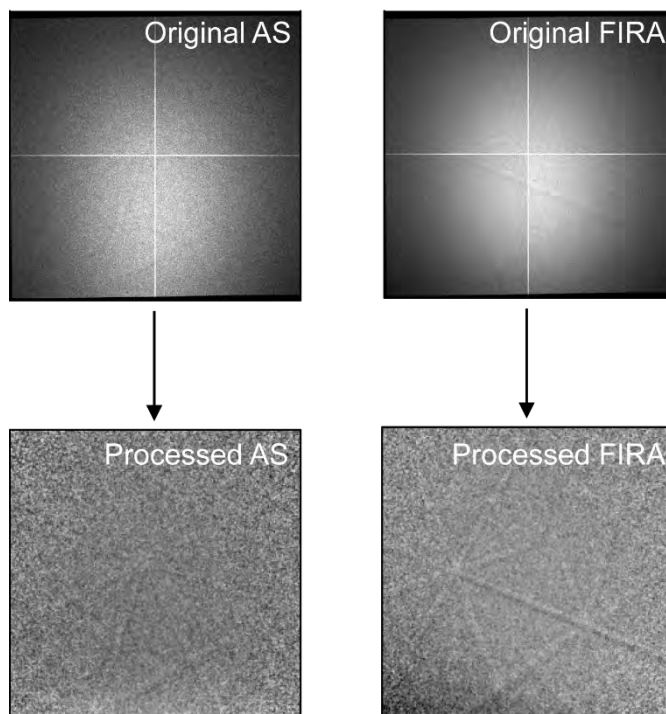


Figure 1.6. *Image processing routine.* Kikuchi patterns taken from reference¹⁰⁹ for MAPbI₃ thin films fabricated via two different strategies before and after image processing.

Calibration is fundamental to obtain reliable data. The goal of the calibration is to establish the geometry of the projection of the EBSD pattern onto the detector and therefore determine the geometrical relationship between the sample coordinates in the SEM chamber and the detector. To calibrate our system, we use a routine which define the calibration parameters using a high-

quality pattern from a known material at a specific working distance (*e.g.* Cu, Al or Si). Specifically, we have measured Kikuchi patterns of copper and silicon at working distances from 10 to 13mm. Then this calibration is applied to the perovskite Kikuchi patterns before indexing. Despite the power of this technique for probing microstructural information of crystalline solids, the detection with a phosphor screen requires high current for the collection of a sufficiently large signal-to-noise ratio due to presence of losses given by the optics present in the collection path. This is a limitation when investigating perovskite thin films, as the use of a current of a few nA can already be damaging to the material. Instead, in this thesis we use a direct-electron detector¹¹² (*i.e.* the phosphor screen is not used), which directly measures the incident electrons onto the detector. Therefore, this type of detector has higher sensitivity compared to the traditional detectors and crucial for probing perovskite's microstructure without altering or damaging the specimen while measuring¹¹³. Here, the current required to collect a sufficient large signal-to-noise ratio signal is in the order of a few pA. The other difference with the traditional EBSD detectors employing phosphor screens is the required accelerating voltage. The traditional one requires a voltage of 15-20 kV that also increases the probing depth. On the other hand, the direct-electron detector can probe the microstructure with adequate signal-to-noise ratio even at 5kV, making the technique more surface sensitive. In addition, the typical acquisition time per pixel necessary to obtain high quality patterns is significantly reduced from a few seconds to a few milliseconds when moving from a phosphor screen-based detector to a direct electron detector.

1.6. Pressure-dependent Spectroscopy

We have already discussed in **Chapter 1.3** and **Chapter 1.4** how the dual ionic-covalent nature of the bond in perovskites is reflected in the mechanically soft and dynamically disordered perovskite lattice. Alterations of the perovskite lattice provide a route to manipulate the electronic landscape of these solids. These alterations can be achieved by chemically replacing the elemental components of the perovskite lattice or by applying an external bias. The aim of this thesis is to investigate how changes in a specific perovskite lattice affects the

1 - Introduction & Background

optical properties without altering the composition. Therefore, the first approach is here excluded. The second approach requires the application of an external bias able to induce a small and continuous change in the atomic structure in order to draw a correlation with a change in the perovskite properties. To date, how changes in temperature affect the perovskite structure are well known and heavily studied^{62,68,114,115}. Changes in temperature include alterations in the crystal lattice constants together with modifications in the phonon distribution, carrier mobility, charges diffusion length. In sharp contrast, changes induced by pressure affect only the perovskite lattice constants and all the following modifications in the optoelectronic landscape can be linked to these structural changes without being affected by pressure in the first place.

Most of the pressure-dependent techniques are based on diamond anvil cell. Here, the sample is placed between small flat faces on the pointy ends of two diamonds and the pressure is generated by applying a force across the faces of the diamonds. One of the main advantages in the use of the diamond anvil cell over other pressure techniques is its transparency to many forms of radiations. The absence of windows between the sample and the radiation source allows the combination of this tool with various light sources. Therefore, X-Ray can be used to characterize the structure of the material, lasers of various wavelengths can be used to study absorption, photoluminescence or other processes in different range of energies. Nowadays, most of the high-pressure material properties known are the result of employing anvil cell-based techniques.

The application of the force across the faces of the diamonds results in a gradient of pressure within the sample, where the highest pressure is experienced in the centre of the sample and the lowest (1 atm) at the edges. Thus, the pressure applied is not isotropic but limited from the force exerted on the diamonds in a particular sample's direction. Since diamonds are inert, this technique is extremely versatile for a wide range of substances, and it works both for powders, films, or liquid provided that the diamonds are not damaged. Gasket and confining media (*e.g.* N₂, Ar, He, ethanol, methanol and NaCl) are also used to reduce the extreme shear stress within the sample and friction between the sample and the diamond face. However, despite their popularity for pressure-dependent structural and spectroscopic measurements, the pressure range accessible through

this type of pressure cell starts at high values, from gigapascals to hundreds of gigapascal. Lower ranges are difficult to access in a controlled way. Lower pressures in the order of 10^{-2} - 10^{-1} GPa are an interesting range to investigate because it aligns with typical values reached during the manufacturing or through chemical and compositional engineering in semiconductor materials. For this reason, in this thesis, we use a hydrostatic pressure cell working in a lower range of pressure (0.05 – 0.4 GPa). The pressure cell consists of a metal housing with transparent windows as shown in **Figure 1.7a**. Depending on the transmission range needed, it is possible to use quartz (180-2000 nm), sapphire (250-5000 nm) or magnesium fluoride (150-6500 nm) as a material for the pressure cell windows, bearing in mind that different materials can handle a different value of maximum pressure. In this thesis, the windows used are quartz, allowing for pressure range from 0 GPa to 0.4 GPa. The pressure cell is filled with a transparent fluorinated mix of inert liquids that are perfluorohexane, dodecafluoro-n-pentane and decafluorobutane. In this thesis, the liquid is abbreviated with his commercial name, FC-72¹¹⁶. The liquid is thermally and chemically stable and compatible with all the perovskites studied in this thesis. Furthermore, it is not toxic and evaporates without leaving residuals on the sample. An important requirement for a liquid to be used as medium in the pressure cell is a negligible absorption in the range of energies used to investigate the material properties. All the measurements conducted in this thesis aim to investigate perovskite properties in the near ultraviolet and the visible. As shown in **Figure 1.7b**, the FC-72 has a flat optical response in this range, making it suitable for the scope of this thesis. However, extra care needs to be taken when measuring at pressure above 0.3 GPa as the liquid become translucent, increasing the scattering and therefore reducing the transmission through the liquid. This effect is due to the presence of O₂ in the liquid. To prevent a significant reduction in transmission when working at high pressure, the liquid is degassed with the *Freeze-Pump-Thaw* cycling in the Schlenk line through which dissolved gases are removed from the liquid. The liquid is first frozen by immersion of the flask in liquid N₂. When completely frozen, the flask is opened to the vacuum and pumped for 3 minutes with the flask still immersed in the liquid N₂. The vacuum is then closed, and the flask is warmed until the solvent has completely melted. This process is repeated for 3

1 - Introduction & Background

times before to disconnect the flask from the Schlenk line and store it in the glovebox to prevent further incorporation of O₂. The pressure is generated by increasing the amount of the liquid in the pressure cell through a pump at a constant volume. An advantage of the use of this hydrostatic pressure cell is the possibility to probe a large area sample (a few cm²) in comparison with the diamond anvil cells (powders or films with volume in the cubic micrometre range). It is worth mentioning that contrary to the diamond anvil cell, the hydrostatic pressure cell applies an isotropic pressure.

a)



b)

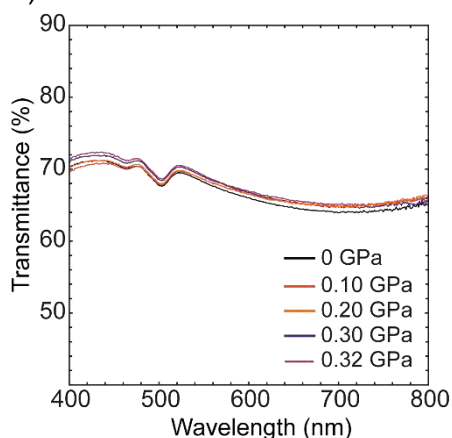


Figure 1.7. *Hydrostatic pressure cell used to compress the perovskite. a)* Hydrostatic pressure cell with quartz windows used in this thesis. The pressure cell is connected to a manual pump. **b)** Transmittance spectrum of the FC-72 shows a relatively flat response in the energy range used in this thesis.

Pressure-dependent optical absorption allows for monitoring the bandgap of materials as a function of the applied pressure. While the bandgap can also be measured using emission spectroscopy, absorption is not only useful in the case of compositions that do not show radiative band-edge transitions at a certain pressure, but also for compositions where several optical bandgaps are present, whereas the emission feature derives only from certain states. For example, this is the case of mixed-halide perovskites under illumination that exhibit phase segregation. During illumination of such materials, iodide- and bromide-rich

domains are formed. Thus, three bandgaps are present in the composition: one can be attributed to the original mixing ratio, one to the bromide-rich phase (high-energy bandgap) and one to the iodide-rich phase (low-energy bandgap). However, the radiative emission of these compositions originates only from the iodide-rich phase that is the low energy state into which charges funnel from the mixed-phase. Thus, the bandgap evolution obtained through pressure-dependent photoluminescence is not complete. In addition, the comparison between absorption and emission can reveal the evolution of the Stokes shift under pressure. Together with the steady-state optical absorption measurements, pressure-dependent transient absorption spectroscopy is a powerful tool to investigate the photogenerated excited state absorption energies and associated lifetimes of perovskites.

In this thesis, we use a femtosecond pressure-dependent transient absorption setup (fs-TAS) where we combine our hydrostatic pressure cell with a non-degenerate pump-probe configuration. The setup is schematically depicted in [Figure 1.8](#). The laser source for the TA is a regenerative Ti:sapphire amplifier (Coherent) generating a fundamental beam characterized by 800-nm pulses at a 1-kHz repetition rate, with a pulse duration of 35 fs and a pulse energy of 6.5 mJ. The fundamental beam is split into two beams by a beam splitter. After chopping the beam in the pump path (using 500 Hz as the frequency), a 400-nm pulse pump is generated by doubling the 800-nm pulse with a beta barium borate (BBO) crystal. This beam is the *pump* and is responsible for the generation of the excited states.

1 - Introduction & Background

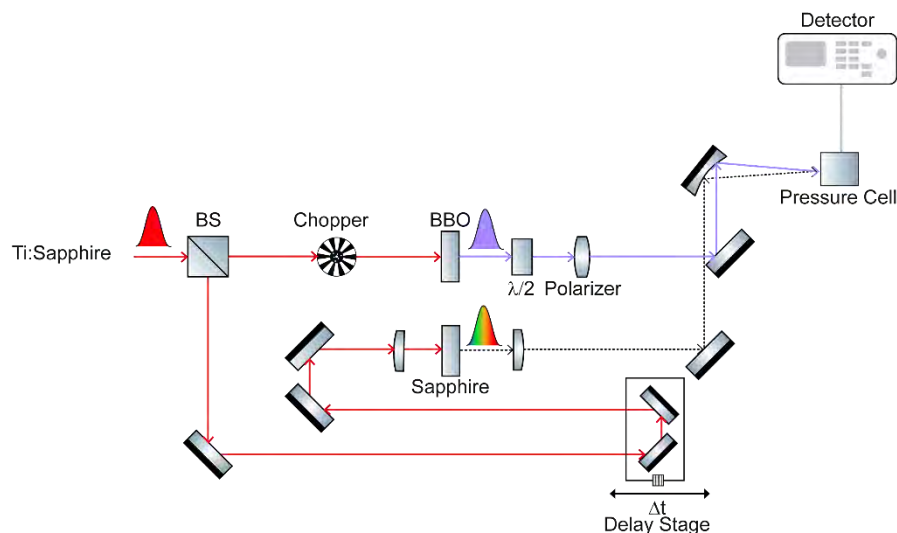


Figure 1.8. Schematic representation of the pressure-dependent transient absorption spectroscopy setup used in this thesis. The laser source (Ti:Sapphire) is split in two beams. The frequency of the first is doubled using a BBO crystal to generate the pump beam (3.1 eV). The second beam is used to generate white light using a sapphire plate. The pump-probe delay is controlled by a mechanical delay stage allowing for probing from 0.05 ps to 800 ps. Pump and probe are focussed on the sample sitting inside the pressure cell through a parabolic mirror.

A short-pass filter is placed after the BBO crystal in the pump path to remove 800-nm residue from the fundamental beam which might cause saturation of the detector during the acquisition and a falsehood of $\Delta T/T$ features in that wavelength range. The white light continuum *probe* pulse is generated by focusing the 800-nm femtosecond pulses through a 2-mm sapphire plate. To prevent two-photon absorption by the sample, which could be excited by the high-density probe, a reflective neutral density filter (OD 1) is placed in the probe path before the sample position.

A 50 cm mechanical delay stage is used to delay the arrival time of the probe with respect to the pump and thus follow the evolution of ultrafast processes as a function of time. The delay time accessible is from 0.05 ps to 800 ps.

Furthermore, it is possible to set a specific delay time and follow in real time (seconds or minutes) the evolution of the investigated system. This functionality will be used later in **Chapter 4** to investigate the phase segregation of mixed-halide perovskites during illumination as a function of real time (minutes) and at a specific delay time, after the hot-carrier cooling process and before charges recombination. The pump beam (3.1 eV) and the probe beam (white light) are overlapped inside the pressure cell during the measurement and the probe spot size was chosen to be smaller than the pump spot size to obtain homogenous excitation over the probed area.

The overlap of the pump and probe beam inside the pressure cell is crucial to collect the $\Delta T/T$ signal and the correct alignment is challenging. The alignment process in the pressure cell, compared to the case of a conventional sample holder in air, is limited by the size of the pressure cell windows whose aperture is 10 mm and the inability of looking directly at the sample while aligning. The first issue is tackled by focusing on the sample both the pump and probe with a parabolic mirror (*i.e.* avoiding two different focussing paths for the two beams). Aligning a parabolic mirror is not straightforward, and the two incoming beams must be parallel to be focussed at the same distance without elliptical distortion of the beam. The second issue is tackled by using a specific alignment strategy which consists of the use of a 3-axis translation stage where the pressure cell sits and a metallic plate of the same size of the sample characterised by a pinhole in the center of about 100 μm . This metallic plate is used as guide for a first rough alignment. First, we move the pressure cell along the x , y and z direction to make the probe beam passing through the pinhole in the metallic plate. This procedure has the scope of aligning the beam in a specific point of the sample. The goodness of the alignment is monitored by looking at the number of counts reaching the detector placed after the pressure cell. When the counts are optimised, the pump beam is moved toward the same position of the probe, this time without moving the pressure cell. When the pump spot is observed after the pressure cell, the first rough alignment is complete, and the metallic plate is replaced by the real specimen. At this stage, pump and probe overlap roughly at the same position. However, a fine tuning is done using the sample to monitor the overlap. When the sample is placed in the pressure cell, we move the mirror before the parabolic

1 - Introduction & Background

mirror that controls the direction of the pump beam to increase the $\Delta T/T$ signal collected by the detector. When the signal is optimised, the sample is ready to be measured. It is worth noting that this alignment procedure is done with the pressure cell liquid as the refractive index of the liquid is higher (1.25) than air (1.00), thus changing the focal point of the beam. The alignment of the pressure-dependent transient absorption setup is fine-tuned at each pressure from ambient to 0.35 GPa by moving the pump beam to optimize the number of counts collected by the detector.

The collected spectrum of the transient species is a measure of the change in the transmittance ΔT of the system after excitation with the pump pulse T_{on} and before excitation T_{off} when the system is in the ground state as in Eq. 1.3. The collected signal can be expressed also using the absorption.

$$\frac{\Delta T}{T} = \frac{T_{on} - T_{off}}{T_{off}} \quad (1.3)$$

The differential spectrum collected at different delay time between pump and probe can track the evolution of the ground and excited states of the material as a function of wavelength and time. **Figure 1.9** shows a simple case of a sample with a ground state (G) and, as example, two excited states (A and B). The differential transmittance spectrum contains much information of the system but in turn it results in a complex convolution of signals:

- *Ground-state bleach (GSB)*: in the unperturbed system (*pump off*), most of the charges are in the ground state (G). When the system is excited by the pump (*pump on*), some of these charges are promoted to the excited level A. Hence, the ground-state transmittance in the excited system is greater than the one in the non-excited system, resulting in a positive signal in the $\Delta T/T$ spectrum in the wavelength region of the ground state absorption as in **Figure 1.9**.
- *Stimulated emission to the ground-state bleach (SE)*: this process occurs when a photon from the probe passes through the excited volume of the sample and induces the emission of another photon from the excited state A of the sample to the ground-state G. The emitted photons have the same

direction of the probe and therefore collected by the detector. As a result, the transmitted light intensity at the detector position will be higher when the pump is on, and the $\Delta T/T$ signal will be positive as in **Figure 1.9**. The energy of the emitted photons roughly matches the photoluminescence spectrum of the sample.

- *Excited state absorption (ESA)*: the pump excitation may induce optical transition from the excited state A to a higher-lying excited state B in certain wavelength regions with a consequent absorption of the probe at these wavelengths. Thus, the transmittance at these wavelengths when the system is excited is lower than when the system is not excited due to the promotion of charges to those energy levels. Therefore, a negative signal in the $\Delta T/T$ spectrum will appear (**Figure 1.9**).

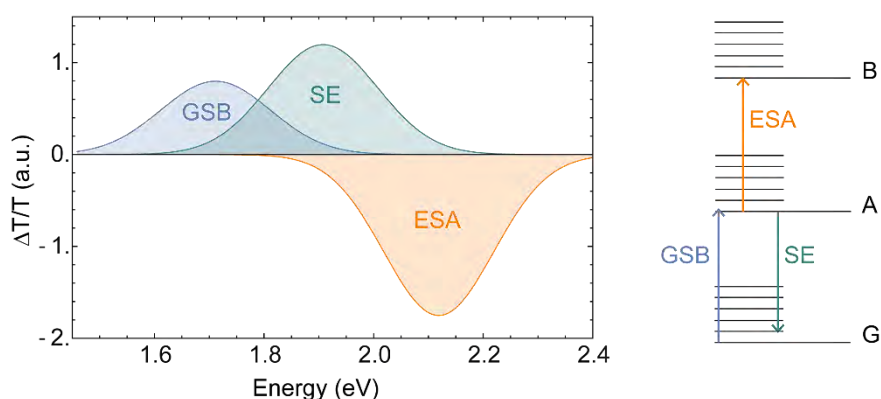


Figure 1.9. Typical features expected in a $\Delta T/T$ spectrum. Schematic representation of the deconvoluted signals observed after collection of TA spectra. On the right, the energy transition associated to the observed features.

A common artifact related to the use of a supercontinuum pulse is the chirp of the white light due to the temporal dispersion of the frequency of the probe. In other words, all the wavelengths of the white light do not reach the sample at the same time (**Figure 1.10a**), resulting in a different time zero (*i.e.* when pump and probe overlap in time) that distorts the $\Delta T/T$ spectrum. The kinetics at a specific wavelength is not affected by this artifact but to monitor precisely the

1 - Introduction & Background

evolution in the picosecond timescale of all the $\Delta T/T$ features, a correction needs to be made. We extract the chirp measuring the arrival time of each wavelength on a bare quartz substrate, the same used as substrate to deposit the perovskites studied in this thesis. The measurement is done inside the pressure cell, with the same optics and in the same conditions as the real experiment. The chirp is not affected by pressure; thus, we use the correction calculated at ambient pressure (~ 3 ps) and the result is shown in **Figure 1.10b**.

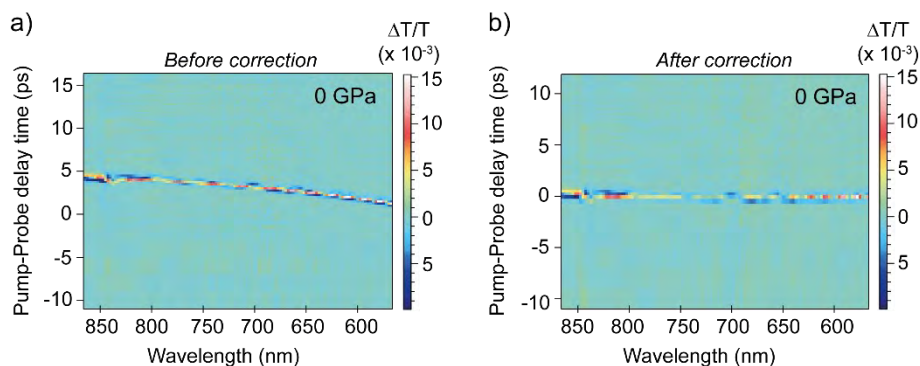


Figure 1.10. Chirp of the white light continuum. **a)** Common artifact when using supercontinuum probe light due to the temporal dispersion (chirp) of the frequency of the probe and **b)** its correction resulting at the same time zero for all the wavelengths of the light.

To date, a broad range of photoluminescence-based techniques have been used to characterise the properties of perovskite¹¹⁴. For instance, pressure- and temperature-dependent PL have been used to investigate phase transitions. Voltage-dependent PL has been used in complete solar cells or LEDs to study the interplay between radiative and non-radiative recombination¹¹⁷. Spatially resolved PL is used to characterise large areas in the perovskite thin films and quantify inhomogeneities relevant for devices¹¹⁸. For a more complete picture of the optical properties of a material, absorption measurements can be combined with pressure-dependent photoluminescence experiments as later discussed in **Chapter 5**. The setup used in this thesis is schematically represented in **Figure 1.11**.

In this thesis, we conduct pressure-dependent photoluminescence measurements using a 405 nm or 375 nm continuous laser (CW) as source of excitation. We then focus the laser on the sample sitting inside the pressure cell at 45° and the reflected signal is collected from a spectrometer operating in the visible. To avoid the saturation of the spectrometer, a 450 nm long pass filter is placed after the pressure cell to filter out the reflection of the laser. The alignment of the pressure-dependent photoluminescence setup is fine-tuned at each pressure from ambient to 0.35 GPa to compensate for slight deviation of the beam with respect to the spectrometer. Exposure time between 0.5 s and 10 s are used depending on the emissivity of the sample.

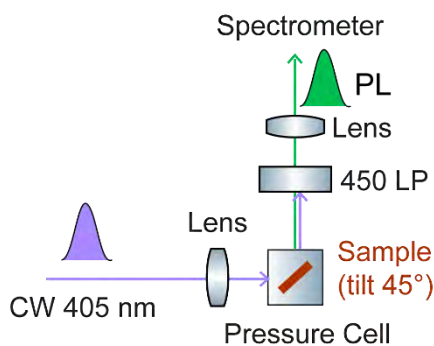


Figure 1.11. *Photoluminescence setup.* Schematic representation of the steady-state photoluminescence setup used in this thesis.

1.7. Outline of the thesis

In this thesis, we focus on investigating the structural response of perovskites to the exertion of external pressure. Due to the strong connection between structural and optoelectronic properties in these materials, external pressure and, more in general, strain, can be used to manipulate the optical properties of these materials targeting specific device applications.

In **Chapter 2** we study the microstructure of methylammonium lead iodide (MAPbI₃) thin films fabricated with the conventional antisolvent-dripping (AS) method and the novel flash-infrared annealing (FIRA) and how this affects

optoelectronic properties such as local photoluminescence (PL), charge carrier lifetimes, and mobilities. To probe the microstructure, we use electron back-scattered diffraction (EBSD), and we find that oftentimes domains observed in SEM are misidentified with crystallographic grains. Despite substantial differences in grain size between the two systems (~100s of nm for the AS and ~100s of μm for the FIRA), we find similar optoelectronic properties suggesting that the optoelectronic quality is not necessarily related to the orientation and size of crystalline domains.

In **Chapter 3** we move to investigate how structural changes in MAPbI_3 thin films induced by external pressure affect its photophysics in the femtosecond timescale. Here, we suggest pressure as a tool to manipulate the hot-carrier cooling for targeting specific applications as hot-carrier solar cells, lasers, thermoelectric devices. A combination of computational analysis and spectroscopic data reveal the role of pressure in the change of electron-phonon coupling which in turn affects the rate at which hot-carriers reach the lattice temperature. Applying compressive stress to the material favours fast hot-carrier cooling at high excitation density ($> 10^{18}$ photons/ cm^2) which would be beneficial for light-emitting diodes (LEDs) and laser applications.

The effect of pressure is noticeable not only in the femtosecond timescale but also in the seconds-minutes timescale. In **Chapter 4** we investigate the phase segregation in mixed-halide perovskites, a detrimental process occurring when mixed-halide compositions are subjected to continuous illumination. This segregation occurs through halide migration, which is also observed in single-halide compositions, and whose control is thus essential to enhance the lifetime and long-term stability of devices. We use pressure-dependent transient absorption spectroscopy in combination with computational calculations to track the evolution of the mixed phase as well as the bromide- and iodide-rich phase in mixed-halide perovskites as a function of real time and pressure. We observe that phase segregation is almost suppressed at 0.3 GPa for several bromide-iodide mixing ratio and also the overall segregation rate is dramatically reduced. Our findings suggest that the process of phase segregation cannot be associated only to thermodynamics or kinetics but a combination of the two is the key towards a better understanding of this process. Furthermore, the pressure reveals itself as an

effective tool to reduce phase segregation. A similar compression of the unit cell volume can be achieved by chemical engineering, specifically replacing the A^+ cation with a smaller ion, exemplified by replacing MA^+ with Cs^+ . Comparably to what obtained under hydrostatic pressure, the change induced by this “*chemical pressure*” reduces the phase segregation.

Layered 2D perovskites offer even a richer parameter space for property manipulations as they consist of an inorganic framework and organic spacer that can be tuned according to the required functionalities. Therefore, external mechanical stimuli, such as pressure, can be used to induce structural changes and investigate the effect on their optical properties. In **Chapter 5** we investigate the structure-property relationship in representative iodide- and bromide-based Ruddlesden-Popper and Dion-Jacobson 2D perovskites fabricated with comparable organic spacers, benzylammonium (BN) and 1,4-phenylenedimethylammonium (PDMA), respectively. By using pressure-dependent absorption and X-ray diffraction (synchrotron source), we probe the correlation between optical and structural properties in the range of 0-0.35 GPa, a pressure at which the observed effects might be comparable to the processes occurring in the optoelectronic devices (*e.g.* polaron induced strain, lattice mismatch, chemical strain) and during manufacturing. We find that Ruddlesden-Popper and Dion-Jacobson perovskites behave similarly under pressure, despite the different forces involved in connecting the two perovskites slabs and there is no difference in the pressure response between the iodide- and bromide-based systems. The only outlier is $(BN)_2PbBr_4$, where we find a larger redshift in the optical absorption under pressure (-54.9 meV). Pressure-dependent X-ray diffraction measurements in combination with density functional theory calculations reveal that the origin of this large shift is the presence of an isostructural phase transition. This phase transition is associated with a decrease in the octahedra tilting (*i.e.* angles closer to 180°) which leads to an increased penetration depth of the BN spacers into the inorganic framework.

1.8. References

- (1) Bai, T.; Yang, B.; Chen, J.; Zheng, D.; Tang, Z.; Wang, X.; Zhao, Y.; Lu, R.; Han, K. Efficient Luminescent Halide Quadruple-Perovskite Nanocrystals via Trap-Engineering for Highly Sensitive Photodetectors. *Adv. Mater.* **2021**, *33* (8). <https://doi.org/10.1002/ADMA.202007215>.
- (2) Wei, F.; Deng, Z.; Sun, S.; Xie, F.; Kieslich, G.; Evans, D. M.; Carpenter, M. A.; Bristowe, P. D.; Cheetham, A. K. The Synthesis, Structure and Electronic Properties of a Lead-Free Hybrid Inorganic–Organic Double Perovskite $(\text{MA})_2\text{KBiCl}_6$. *Mater. Horizons* **2016**, *3* (4). <https://doi.org/10.1039/C6MH00053C>.
- (3) Liang, K.; Mitzi, D. B.; Prikas, M. T. Synthesis and Characterization of Organic-Inorganic Perovskite Thin Films Prepared Using a Versatile Two-Step Dipping Technique. *Chem. Mater.* **1998**, *10* (1). <https://doi.org/10.1021/cm970568f>.
- (4) Mitzi, D. B. Templating and Structural Engineering in Organic-Inorganic Perovskites. *J. Chem. Soc., Dalt. Trans* **2001**, *1* (12). <https://doi.org/10.1039/b007070j>.
- (5) Mao, L.; Ke, W.; Pedesseau, L.; Wu, Y.; Katan, C.; Even, J.; Wasielewski, M. R.; Stoumpos, C. C.; Kanatzidis, M. G. Hybrid Dion–Jacobson 2D Lead Iodide Perovskites. *J. Am. Chem. Soc.* **2018**, *140*, 47. <https://doi.org/10.1021/jacs.8b00542>.
- (6) Stoumpos, C. C.; Cao, D. H.; Clark, D. J.; Young, J.; Rondinelli, J. M.; Jang, J. I.; Hupp, J. T.; Kanatzidis, M. G. Ruddlesden – Popper Hybrid Lead Iodide Perovskite 2D Homologous Semiconductors. *Chem. Mater.* **2016**, *28*. <https://doi.org/10.1021/acs.chemmater.6b00847>.
- (7) Kong, L.; Liu, G.; Gong, J.; Mao, L.; Chen, M.; Hu, Q.; Lü, X.; Yang, W.; Kanatzidis, M. G.; Mao, H. K. Highly Tunable Properties in Pressure-Treated Two-Dimensional Dion–Jacobson Perovskites. *Proc. Natl. Acad. Sci. U. S. A.* **2020**, *117* (28). <https://doi.org/10.1073/pnas.2003561117>.
- (8) Chen, Y.; Zhang, L.; Zhang, Y.; Gao, H.; Yan, H. Large-Area Perovskite Solar Cells – a Review of Recent Progress and Issues. *RSC Adv.* **2018**, *8* (19). <https://doi.org/10.1039/C8RA00384J>.
- (9) Nie, W. Y.; Tsai, H. H.; Asadpour, R.; Blancon, J.-C. C. J.-C. J.-C. C.; Neukirch, A. J.; Gupta, G.; Crochet, J. J.; Chhowalla, M.; Tretiak, S.; Alam, M. A.; et al. High-Efficiency Solution-Processed Perovskite Solar Cells with Millimeter-Scale Grains. *Science* **2015**, *347* (6221). <https://doi.org/10.1126/science.aaa0472>.
- (10) Eperon, G. E.; Stranks, S. D.; Menelaou, C.; Johnston, M. B.; Herz, L. M.; Snaith, H. J. Formamidinium Lead Trihalide: A Broadly Tunable Perovskite for Efficient Planar Heterojunction Solar Cells. *Energy Environ. Sci.* **2014**, *7* (3). <https://doi.org/10.1039/c3ee43822h>.

- (11) Noh, J. H.; Im, S. H.; Heo, J. H.; Mandal, T. N.; Seok, S. Il. Chemical Management for Colorful, Efficient, and Stable Inorganic–Organic Hybrid Nanostructured Solar Cells. *Nano Lett.* **2013**, *13* (4). <https://doi.org/10.1021/nl400349b>.
- (12) Sadhanala, A.; Ahmad, S.; Zhao, B.; Giesbrecht, N.; Pearce, P. M.; Deschler, F.; Z Hoye, R. L.; Go, K. C.; Bein, T.; Docampo, P.; et al. Blue-Green Color Tunable Solution Processable Organolead Chloride–Bromide Mixed Halide Perovskites for Optoelectronic Applications. *Nano Lett.* **2015**, *15* (6101). <https://doi.org/10.1021/acs.nanolett.5b02369>.
- (13) Amat, A.; Mosconi, E.; Ronca, E.; Quarti, C.; Umari, P.; Nazeeruddin, M. K.; Grätzel, M.; De Angelis, F. Cation-Induced Band-Gap Tuning in Organohalide Perovskites: Interplay of Spin-Orbit Coupling and Octahedra Tilting. *Nano Lett.* **2014**, *14* (6). <https://doi.org/10.1021/NL5012992>.
- (14) Pazos-Outón, L. M.; Xiao, T. P.; Yablonovitch, E. Fundamental Efficiency Limit of Lead Iodide Perovskite Solar Cells. *J. Phys. Chem. Lett.* **2018**, *9* (7). <https://doi.org/10.1021/acs.jpcclett.7b03054>.
- (15) Wang, Q.; Wang, X.; Yang, Z.; Zhou, N.; Deng, Y.; Zhao, J.; Xiao, X.; Rudd, P.; Moran, A.; Yan, Y.; et al. Efficient Sky-Blue Perovskite Light-Emitting Diodes via Photoluminescence Enhancement. *Nat. Commun.* **2019**, *10* (1). <https://doi.org/10.1038/s41467-019-13580-w>.
- (16) Sarritzu, V.; Sestu, N.; Marongiu, D.; Chang, X.; Masi, S.; Rizzo, A.; Colella, S.; Quochi, F.; Saba, M.; Mura, A.; et al. Optical Determination of Shockley-Read-Hall and Interface Recombination Currents in Hybrid Perovskites. *Sci. Rep.* **2017**, *7* (44629). <https://doi.org/10.1002/adom.201700839>.
- (17) Ball, J. M.; Petrozza, A. Defects in Perovskite-Halides and Their Effects in Solar Cells. *Nat. Energy* **2016**, *1* (16149). <https://doi.org/10.1038/nenergy.2016.149>.
- (18) Meggiolaro, D.; De Angelis, F. First-Principles Modeling of Defects in Lead Halide Perovskites: Best Practices and Open Issues. *ACS Energy Lett.* **2018**, *3* (9). <https://doi.org/10.1021/acsenerylett.8b01212>.
- (19) Das, B.; Liu, Z.; Aguilera, I.; Rau, U.; Kirchartz, T. Defect Tolerant Device Geometries for Lead-Halide Perovskites. *Mater. Adv.* **2021**, *2* (11). <https://doi.org/10.1039/d0ma00902d>.
- (20) Kim, G. W.; Petrozza, A. Defect Tolerance and Intolerance in Metal-Halide Perovskites. *Adv. Energy Mater.* **2020**, *10* (37). <https://doi.org/10.1002/AENM.202001959>.
- (21) Pisoni, A.; Jaćimović, J.; Barišić, O. S.; Spina, M.; Gaál, R.; Forró, L.; Horváth, E. Ultra-Low Thermal Conductivity in Organic-Inorganic Hybrid Perovskite $\text{CH}_3\text{NH}_3\text{PbI}_3$. *J. Phys. Chem. Lett.* **2014**, *5* (14). <https://doi.org/10.1021/jz5012109>.

- (22) Kovalsky, A.; Wang, L.; Marek, G. T.; Burda, C.; Dyck, J. S. Thermal Conductivity of $\text{CH}_3\text{NH}_3\text{PbI}_3$ and CsPbI_3 : Measuring the Effect of the Methylammonium Ion on Phonon Scattering. *J. Phys. Chem. C* **2017**, *121* (6). <https://doi.org/10.1021/acs.jpcc.6b12231>.
- (23) Kanak, A.; Lishchuk, P.; Kuryliuk, V.; Kuzmich, A.; Lacroix, D.; Khalavka, Y.; Isaiev, M. Thermal Conductivity of CsPbBr_3 Halide Perovskite: Photoacoustic Measurements and Molecular Dynamics Analysis. *AIP Conf. Proc.* **2020**, *2305* (1). <https://doi.org/10.1063/5.0033821>.
- (24) Pisoni, A.; Jaćimović, J.; Barišić, O. S.; Spina, M.; Gaál, R.; Forró, L.; Horváth, E. Ultra-Low Thermal Conductivity in Organic-Inorganic Hybrid Perovskite $\text{CH}_3\text{NH}_3\text{PbI}_3$. *J. Phys. Chem. Lett.* **2014**, *5* (14). <https://doi.org/10.1021/jz5012109>.
- (25) Mei, S.; Knezevic, I. Thermal Conductivity of Ternary III-V Semiconductor Alloys: The Role of Mass Difference and Long-Range Order. *J. Appl. Phys.* **2018**, *123* (12). <https://doi.org/10.1063/1.5008262>.
- (26) Leturcq, P.; Dorkel, J. M.; Napieralski, A.; Lachiver, E. A New Approach to Thermal Analysis of Power Devices. *IEEE Trans. Electron Devices* **1987**, *34* (5). <https://doi.org/10.1109/T-ED.1987.23057>.
- (27) Spitzer, D. P. Lattice Thermal Conductivity of Semiconductors: A Chemical Bond Approach. *J. Phys. Chem. Solids* **1970**, *31* (1). [https://doi.org/10.1016/0022-3697\(70\)90284-2](https://doi.org/10.1016/0022-3697(70)90284-2).
- (28) Gold-Parker, A.; Gehring, P. M.; Skelton, J. M.; Smith, I. C.; Parshall, D.; Frost, J. M.; Karunadasa, H. I.; Walsh, A.; Toney, M. F. Acoustic Phonon Lifetimes Limit Thermal Transport in Methylammonium Lead Iodide. *Proc. Natl. Acad. Sci. U. S. A.* **2018**, *115* (47). <https://doi.org/10.1073/pnas.1812227115>.
- (29) Bakulin, A. A.; Selig, O.; Bakker, H. J.; Rezus, Y. L. A.; Müller, C.; Glaser, T.; Lovrincic, R.; Sun, Z.; Chen, Z.; Walsh, A.; et al. Real-Time Observation of Organic Cation Reorientation in Methylammonium Lead Iodide Perovskites. *J. Phys. Chem. Lett.* **2015**, *6* (18). <https://doi.org/10.1021/ACS.JPCLETT.5B01555>.
- (30) Fabini, D. H.; Siaw, T. A.; Stoumpos, C. C.; Laurita, G.; Olds, D.; Page, K.; Hu, J. G.; Kanatzidis, M. G.; Han, S.; Seshadri, R. Universal Dynamics of Molecular Reorientation in Hybrid Lead Iodide Perovskites. *J. Am. Chem. Soc.* **2017**, *139* (46). <https://doi.org/10.1021/JACS.7B09536>.
- (31) Haque, M. A.; Kee, S.; Villalva, D. R.; Ong, W. L.; Baran, D. Halide Perovskites: Thermal Transport and Prospects for Thermoelectricity. *Advanced Science*. **2020**, *7*, (10). <https://doi.org/10.1002/advs.201903389>.
- (32) Fu, J.; Xu, Q.; Han, G.; Wu, B.; Huan, C. H. A.; Leek, M. L.; Sum, T. C. Hot Carrier Cooling Mechanisms in Halide Perovskites. *Nat. Commun.*

- 2017**, 8 (1). <https://doi.org/10.1038/s41467-017-01360-3>.
- (33) Lim, J. W. M.; Giovanni, D.; Righetto, M.; Feng, M.; Mhaisalkar, S. G.; Mathews, N.; Sum, T. C. Hot Carriers in Halide Perovskites: How Hot Truly? *J. Phys. Chem. Lett.* **2020**, 11 (7). <https://doi.org/10.1021/acs.jpcllett.0c00504>.
- (34) Shen, Q.; Ripolles, T. S.; Even, J.; Ogomi, Y.; Nishinaka, K.; Izuishi, T.; Nakazawa, N.; Zhang, Y.; Ding, C.; Liu, F.; et al. Slow Hot Carrier Cooling in Cesium Lead Iodide Perovskites. *Appl. Phys. Lett.* **2017**, 111 (15). <https://doi.org/10.1063/1.4991993>.
- (35) Fehse, R.; Tomić, S.; Adams, A. R.; Sweeney, S. J.; O'Reilly, E. P.; Andreev, A.; Riechert, H. A Quantitative Study of Radiative, Auger, and Defect Related Recombination Processes in 1.3-Mm GaInNAS-Based Quantum-Well Lasers. *IEEE J. Sel. Top. Quantum Electron.* **2002**, 8 (4). <https://doi.org/10.1109/JSTQE.2002.801684>.
- (36) Righetto, M.; Lim, S. S.; Giovanni, D.; Lim, J. W. M.; Zhang, Q.; Ramesh, S.; Tay, Y. K. E.; Sum, T. C. Hot Carriers Perspective on the Nature of Traps in Perovskites. *Nat. Commun.* **2020**, 11 (1). <https://doi.org/10.1038/s41467-020-16463-7>.
- (37) Walsh, A. Principles of Chemical Bonding and Band Gap Engineering in Hybrid Organic–Inorganic Halide Perovskites. *J. Phys. Chem. C* **2015**, 119 (11). <https://doi.org/10.1021/jp512420b>.
- (38) Brivio, F.; Walker, A. B.; Walsh, A. Structural and Electronic Properties of Hybrid Perovskites for High-Efficiency Thin-Film Photovoltaics from First-Principles. *APL Mater.* **2013**, 1 (4). <https://doi.org/10.1063/1.4824147>.
- (39) Lee, J. H.; Lee, J.-H.; Kong, E.-H.; Jang, H. M. The Nature of Hydrogen-Bonding Interaction in the Prototypic Hybrid Halide Perovskite, Tetragonal CH₃NH₃PbI₃. *Sci. Reports* 2016 61 **2016**, 6 (1). <https://doi.org/10.1038/srep21687>.
- (40) Walsh, A.; Scanlon, D. O.; Chen, S.; Gong, X. G.; Wei, S.-H. H. Self-Regulation Mechanism for Charged Point Defects in Hybrid Halide Perovskites. *Angew. Chemie Int. Ed.* **2015**, 54 (6). <https://doi.org/10.1002/anie.201409740>.
- (41) Li, C.; Guerrero, A.; Huettner, S.; Bisquert, J. Unravelling the Role of Vacancies in Lead Halide Perovskite through Electrical Switching of Photoluminescence. *Nat. Commun.* **2018**, 9 (1). <https://doi.org/10.1038/s41467-018-07571-6>.
- (42) Meggiolaro, D.; Mosconi, E.; Angelis, F. De. Formation of Surface Defects Dominates Ion Migration in Lead-Halide Perovskites. *ACS Energy Lett.* **2019**, 4 (3). <https://doi.org/10.1021/ACSENERGYLETT.9B00247>.
- (43) Futscher, M. H.; Lee, J. M.; McGovern, L.; Muscarella, L. A.; Wang, T.; Haider, M. I.; Fakharuddin, A.; Schmidt-Mende, L.; Ehrler, B.

- Quantification of Ion Migration in $\text{CH}_3\text{NH}_3\text{PbI}_3$ Perovskite Solar Cells by Transient Capacitance Measurements. *Mater. Horizons* **2019**, *6* (7). <https://doi.org/10.1039/c9mh00445a>.
- (44) Lee, J. W.; Kim, S. G.; Yang, J. M.; Yang, Y.; Park, N. G. Verification and Mitigation of Ion Migration in Perovskite Solar Cells. *APL Mater.* **2019**, *7* (4). <https://doi.org/10.1063/1.5085643>.
- (45) Yuan, H.; Debroye, E.; Janssen, K.; Naiki, H.; Steuwe, C.; Lu, G.; Moris, M.; Orgiu, E.; Uji-I, H.; De Schryver, F.; et al. Degradation of Methylammonium Lead Iodide Perovskite Structures through Light and Electron Beam Driven Ion Migration. *J. Phys. Chem. Lett.* **2016**, *7* (3). <https://doi.org/10.1021/acs.jpcllett.5b02828>.
- (46) Nandal, V.; Nair, P. R. Predictive Modeling of Ion Migration Induced Degradation in Perovskite Solar Cells. *ACS Nano* **2017**, *11* (11). <https://doi.org/10.1021/ACS.NANO.7B06294>.
- (47) Azpiroz, J. M.; Mosconi, E.; Bisquert, J.; De Angelis, F. Defects Migration in Methylammonium Lead Iodide and Their Role in Perovskite Solar Cells Operation. *Energy Environ. Sci.* **2015**, *8* (7). <https://doi.org/10.1039/C5EE01265A>.
- (48) Eames, C.; Frost, J. M.; Barnes, P. R. F.; O'Regan, B. C.; Walsh, A.; Islam, M. S. Ionic Transport in Hybrid Lead Iodide Perovskite Solar Cells. *Nat. Commun.* **2015**, *6* (1), 1–8. <https://doi.org/10.1038/ncomms8497>.
- (49) Delugas, P.; Caddeo, C.; Filippetti, A.; Mattoni, A. Thermally Activated Point Defect Diffusion in Methylammonium Lead Trihalide: Anisotropic and Ultrahigh Mobility of Iodine. *J. Phys. Chem. Lett.* **2016**, *7* (13). <https://doi.org/10.1021/ACS.JPCLETT.6B00963>.
- (50) Haruyama, J.; Sodeyama, K.; Han, L.; Tateyama, Y. First-Principles Study of Ion Diffusion in Perovskite Solar Cell Sensitizers. *J. Am. Chem. Soc.* **2015**, *137* (32). <https://doi.org/10.1021/JACS.5B03615>.
- (51) Meloni, S.; Moehl, T.; Tress, W.; Franckeviius, M.; Saliba, M.; Lee, Y. H.; Gao, P.; Nazeeruddin, M. K.; Zakeeruddin, S. M.; Rothlisberger, U.; et al. Ionic Polarization-Induced Current-Voltage Hysteresis in $\text{CH}_3\text{NH}_3\text{PbX}_3$ Perovskite Solar Cells. *Nat. Commun.* **2016**, *7* (1). <https://doi.org/10.1038/ncomms10334>.
- (52) Slotcavage, D. J.; Karunadasa, H. I.; McGehee, M. D. Light-Induced Phase Segregation in Halide-Perovskite Absorbers. *ACS Energy Letters.* **2016**, *1* (6). <https://doi.org/10.1021/acsenerylett.6b00495>.
- (53) Hoke, E. T.; Slotcavage, D. J.; Dohner, E. R.; Bowring, A. R.; Karunadasa, H. I.; McGehee, M. D. Reversible Photo-Induced Trap Formation in Mixed-Halide Hybrid Perovskites for Photovoltaics. *Chem. Sci.* **2015**, *6* (1). <https://doi.org/10.1039/c4sc03141e>.
- (54) Tang, X.; van den Berg, M.; Gu, E.; Horneber, A.; J. Matt, G.; Osvet, A.; J. Meixner, A.; Zhang, D.; J. Brabec, C. Local Observation of Phase

- Segregation in Mixed-Halide Perovskite. *Nano Lett.* **2018**, *18* (3). <https://doi.org/10.1021/acs.nanolett.8b00505>.
- (55) Frost, J. M.; Whalley, L. D.; Walsh, A. Slow Cooling of Hot Polarons in Halide Perovskite Solar Cells. *ACS Energy Lett.* **2017**, *2* (12). <https://doi.org/10.1021/acsenergylett.7b00862>.
- (56) Bretschneider, S. A.; Ivanov, I.; Wang, H. I.; Miyata, K.; Zhu, X.; Bonn, M. Quantifying Polaron Formation and Charge Carrier Cooling in Lead-Iodide Perovskites. *Adv. Mater.* **2018**, *30* (29). <https://doi.org/10.1002/adma.201707312>.
- (57) Zhu, X. Y.; Podzorov, V. Charge Carriers in Hybrid Organic-Inorganic Lead Halide Perovskites Might Be Protected as Large Polarons. *J. Phys. Chem. Lett.* **2015**, *6* (23). <https://doi.org/10.1021/acs.jpcclett.5b02462>.
- (58) Tan, H.; Che, F.; Wei, M.; Zhao, Y.; Saidaminov, M. I.; Todorović, P.; Broberg, D.; Walters, G.; Tan, F.; Zhuang, T.; et al. Dipolar Cations Confer Defect Tolerance in Wide-Bandgap Metal Halide Perovskites. *Nat. Commun.* **2018**, *9* (1). <https://doi.org/10.1038/s41467-018-05531-8>.
- (59) Bischak, C. G.; Hetherington, C. L.; Wu, H.; Aloni, S.; Ogletree, D. F.; Limmer, D. T.; Ginsberg, N. S. Origin of Reversible Photoinduced Phase Separation in Hybrid Perovskites. *Nano Lett.* **2017**, *17* (2). <https://doi.org/10.1021/acs.nanolett.6b04453>.
- (60) Rehman, W.; McMeekin, D. P.; Patel, J. B.; Milot, R. L.; Johnston, M. B.; Snaith, H. J.; Herz, L. M. Photovoltaic Mixed-Cation Lead Mixed-Halide Perovskites: Links between Crystallinity, Photo-Stability and Electronic Properties. *Energy Environ. Sci.* **2017**, *10* (1). <https://doi.org/10.1039/c6ee03014a>.
- (61) Bischak, C. G. G.; Wong, A. B.; Lin, E.; Limmer, D. T.; Yang, P.; Ginsberg, N. S. Tunable Polaron Distortions Control the Extent of Halide Demixing in Lead Halide Perovskites. *J. Phys. Chem. Lett.* **2018**, *9* (14). <https://doi.org/10.1021/acs.jpcclett.8b01512>.
- (62) Lioliou, G.; Meng, X.; Ng, J. S.; Barnett, A. M. Temperature Dependent Characterization of Gallium Arsenide X-Ray Mesa p-i-n Photodiodes. *J. Appl. Phys.* **2016**, *119* (12). <https://doi.org/10.1063/1.4944892>.
- (63) Navarro-Urrios, D.; Colombano, M. F.; Maire, J.; Chávez-Ángel, E.; Arregui, G.; Capuj, N. E.; Devos, A.; Griol, A.; Bellieres, L.; Martínez, A.; et al. Properties of Nanocrystalline Silicon Probed by Optomechanics. *Nanophotonics* **2020**, *9* (16). <https://doi.org/10.1515/NANOPH-2020-0489>.
- (64) Ono, S.; Kikegawa, T. Phase Transformation of GaAs at High Pressures and Temperatures. *J. Phys. Chem. Solids* **2018**, *113*. <https://doi.org/10.1016/J.JPCS.2017.10.005>.
- (65) Brennan, K. F.; Brown, A. S. Magnetic Field Effects in Semiconductors. *Theory Mod. Electron. Semicond. Devices* **2003**.

- <https://doi.org/10.1002/0471224618.CH9>.
- (66) Chang, K.; Xia, J.-B. The Effects of Electric Field on the Electronic Structure of a Semiconductor Quantum Dot. *J. Appl. Phys.* **1998**, *84* (3). <https://doi.org/10.1063/1.368207>.
- (67) Hutter, E. M.; Savenije, T. J. Thermally Activated Second-Order Recombination Hints toward Indirect Recombination in Fully Inorganic CsPbI₃ Perovskites. *ACS Energy Lett.* **2018**, *3* (9). <https://doi.org/10.1021/ACSENERGYLETT.8B01106>.
- (68) Hutter, E. M.; Gélvez-Rueda, M. C.; Osharov, A.; Bulović, V.; Grozema, F. C.; Stranks, S. D.; Savenije, T. J. Direct-Indirect Character of the Bandgap in Methylammonium Lead Iodide Perovskite. *Nat. Mater.* **2017**, *16* (1). <https://doi.org/10.1038/nmat4765>.
- (69) Thouin, F.; Valverde-Chávez, D. A.; Quarti, C.; Cortecchia, D.; Bargigia, I.; Beljonne, D.; Petrozza, A.; Silva, C.; Srimath Kandada, A. R. Phonon Coherences Reveal the Polaronic Character of Excitons in Two-Dimensional Lead Halide Perovskites. *Nat. Mater.* **2019**, *184* **2019**, *18* (4). <https://doi.org/10.1038/s41563-018-0262-7>.
- (70) Mauck, C. M.; France-Lanord, A.; Oendra, A. C. H.; Dahod, N. S.; Grossman, J. C.; Tisdale, W. A. Inorganic Cage Motion Dominates Excited-State Dynamics in 2D-Layered Perovskites (C_xH_{2x+1}NH₃)₂PbI₄ (x = 4–9). *J. Phys. Chem. C* **2019**, *123* (45). <https://doi.org/10.1021/ACS.JPCC.9B07933>.
- (71) Francisco-López, A.; Charles, B.; Weber, O. J.; Alonso, M. I.; Garriga, M.; Campoy-Quiles, M.; Weller, M. T.; Goñi, A. R. Pressure-Induced Locking of Methylammonium Cations versus Amorphization in Hybrid Lead Iodide Perovskites. *J. Phys. Chem. C* **2018**, *122* (38). <https://doi.org/10.1021/acs.jpcc.8b05188>.
- (72) Jaffe, A.; Lin, Y.; L. Mao, W.; I. Karunadasa, H. Pressure-Induced Conductivity and Yellow-to-Black Piezochromism in a Layered Cu–Cl Hybrid Perovskite. *J. Am. Chem. Soc.* **2015**, *137* (4). <https://doi.org/10.1021/ja512396m>.
- (73) Yin, T.; Liu, B.; Yan, J.; Fang, Y.; Chen, M.; Chong, W. K.; Jiang, S.; Kuo, J. L.; Fang, J.; Liang, P.; et al. Pressure-Engineered Structural and Optical Properties of Two-Dimensional (C₄H₉NH₃)₂PbI₄ Perovskite Exfoliated Nm-Thin Flakes. *J. Am. Chem. Soc.* **2019**, *141* (3). <https://doi.org/10.1021/jacs.8b07765>.
- (74) Liu, S.; Sun, S.; Kwan Gan, C.; Granados del Águila, A.; Fang, Y.; Xing, J.; Thu Ha Do, T.; White, T. J.; Li, H.; Huang, W.; et al. Manipulating Efficient Light Emission in Two-Dimensional Perovskite Crystals by Pressure-Induced Anisotropic Deformation. *Sci. Adv.* **2019**, *5* (7). <https://doi.org/10.1126/sciadv.aav9445>.
- (75) Meloni, S.; Palermo, G.; Ashari-Astani, N.; Grätzel, M.; Rothlisberger, U. Valence and Conduction Band Tuning in Halide Perovskites for Solar Cell

- Applications. *J. Mater. Chem. A* **2016**, *4* (41). <https://doi.org/10.1039/c6ta04949d>.
- (76) Pazoki, M.; Jacobsson, T. J.; Hagfeldt, A.; Boschloo, G.; Edvinsson, T. Effect of Metal Cation Replacement on the Electronic Structure of Metalorganic Halide Perovskites: Replacement of Lead with Alkaline-Earth Metals. *Phys. Rev. B* **2016**, *93* (14). <https://doi.org/10.1103/PhysRevB.93.144105>.
- (77) Butler, K. T.; Frost, J. M.; Walsh, A. Band Alignment of the Hybrid Halide Perovskites $\text{CH}_3\text{NH}_3\text{PbCl}_3$, $\text{CH}_3\text{NH}_3\text{PbBr}_3$ and $\text{CH}_3\text{NH}_3\text{PbI}_3$. *Mater. Horizons* **2015**, *2* (2). <https://doi.org/10.1039/C4MH00174E>.
- (78) Yin, W.-J.; Shi, T.; Yan, Y. Unusual Defect Physics in $\text{CH}_3\text{NH}_3\text{PbI}_3$ Perovskite Solar Cell Absorber, *Appl. Phys. Lett.*, **2014**, *104* (6). <https://doi.org/10.1063/1.4864778>.
- (79) Lee, J. H.; Bristowe, N. C.; Lee, J. H.; Lee, S. H.; Bristowe, P. D.; Cheetham, A. K.; Jang, H. M. Resolving the Physical Origin of Octahedral Tilting in Halide Perovskites. *Chem. Mater.* **2016**, *28* (12). <https://doi.org/10.1021/acs.chemmater.6b00968>.
- (80) Jaffe, A.; Lin, Y.; Beavers, C. M.; Voss, J.; Mao, W. L.; Karunadasa, H. I. High-Pressure Single-Crystal Structures of 3D Lead-Halide Hybrid Perovskites and Pressure Effects on Their Electronic and Optical Properties. *ACS Cent. Sci.* **2016**, *2* (4). <https://doi.org/10.1021/acscentsci.6b00055>.
- (81) Liu, G.; Gong, J.; Kong, L.; Schaller, R. D.; Hu, Q.; Liu, Z.; Yan, S.; Yang, W.; Stoumpos, C. C.; Kanatzidis, M. G.; et al. Isothermal Pressure-Derived Metastable States in 2D Hybrid Perovskites Showing Enduring Bandgap Narrowing. *Proc. Natl. Acad. Sci. U. S. A.* **2018**, *115* (32). <https://doi.org/10.1073/pnas.1809167115>.
- (82) Jaffe, A.; Lin, Y.; Karunadasa, H. I. Halide Perovskites under Pressure: Accessing New Properties through Lattice Compression. *ACS Energy Lett.* **2017**, *2* (7). <https://doi.org/10.1021/acscenergylett.7b00284>.
- (83) Liu, S.; Sun, S.; Gan, C. K.; Del Águila, A. G.; Fang, Y.; Xing, J.; Thu Ha Do, T.; White, T. J.; Li, H.; Huang, W.; et al. Manipulating Efficient Light Emission in Two-Dimensional Perovskite Crystals by Pressure-Induced Anisotropic Deformation. *Sci. Adv.* **2019**, *5* (7). <https://doi.org/10.1126/sciadv.aav9445>.
- (84) Tu, Q.; Spanopoulos, I.; Vasileiadou, E. S.; Li, X.; Kanatzidis, M. G.; Shekhawat, G. S.; Dravid, V. P. Exploring the Factors Affecting the Mechanical Properties of 2D Hybrid Organic-Inorganic Perovskites. *ACS Appl. Mater. Interfaces* **2020**, *12* (18). <https://doi.org/10.1021/acscami.0c02313>.
- (85) Tu, Q.; Spanopoulos, I.; Hao, S.; Wolverton, C.; Kanatzidis, M. G.; Shekhawat, G. S.; Dravid, V. P. Out-of-Plane Mechanical Properties of 2D Hybrid Organic-Inorganic Perovskites by Nanoindentation. *ACS Appl.*

- Mater. Interfaces* **2018**, *10* (26). <https://doi.org/10.1021/acsami.8b05138>.
- (86) Gao, H.; Wei, W.; Li, L.; Tan, Y.; Tang, Y. Mechanical Properties of a 2D Lead-Halide Perovskite, $(\text{C}_6\text{H}_5\text{CH}_2\text{NH}_3)_2\text{PbCl}_4$ by Nanoindentation and First-Principles Calculations. *J. Phys. Chem. C* **2020**, *124* (35). <https://doi.org/10.1021/acs.jpcc.0c04283>.
- (87) Xu, B.; Wang, Q.; Tian, Y. Bulk Modulus for Polar Covalent Crystals. **2013**, *3*. <https://doi.org/10.1038/srep03068>.
- (88) Kamran, S.; Chen, K.; Chen, L. Semiempirical Formulae for Elastic Moduli and Brittleness of Diamondlike and Zinc-Blende Covalent Crystals, *Appl. Phys. Lett.*, **2008**, *77* (9). <https://doi.org/10.1103/PhysRevB.77.094109>.
- (89) Menčík, J.; Munz, D.; Quandt, E.; Weppelmann, E. R.; Swain, M. V. Determination of Elastic Modulus of Thin Layers Using Nanoindentation. *J. Mater. Res.* **1997**, *12* (9). <https://doi.org/10.1557/JMR.1997.0327>.
- (90) Kim, M. T. Influence of Substrates on the Elastic Reaction of Films for the Microindentation Tests. *Thin Solid Films* **1996**, *283* (1–2). [https://doi.org/10.1016/0040-6090\(95\)08498-3](https://doi.org/10.1016/0040-6090(95)08498-3).
- (91) Ahmed, R.; Javad Hashemifar, S.; Akbarzadeh, H.; Ahmed, M.; Fazal-e-Aleem. Ab Initio Study of Structural and Electronic Properties of III-Arsenide Binary Compounds. *Comput. Mater. Sci.* **2007**, *39* (3). <https://doi.org/10.1016/J.COMMATSCI.2006.08.014>.
- (92) S. M. SZE. Semiconductor Devices Physics and Technology 3rd Edition.
- (93) Ferreira, A. C.; Létoublon, A.; Paofai, S.; Raymond, S.; Ecolivet, C.; Rufflé, B.; Cordier, S.; Katan, C.; Saidaminov, M. I.; Zhumekenov, A. A.; et al. Elastic Softness of Hybrid Lead Halide Perovskites. *Phys. Rev. Lett.* **2018**, *121* (8). <https://doi.org/10.1103/PhysRevLett.121.085502>.
- (94) Rakita, Y.; Cohen, S. R.; Kedem, N. K.; Hodes, G.; Cahen, D. Mechanical Properties of APbX_3 (A = Cs or CH_3NH_3 ; X = I or Br) Perovskite Single Crystals. *MRS Commun.* **2015**, *5* (4). <https://doi.org/10.1557/mrc.2015.69>.
- (95) Sun, S.; Fang, Y.; Kieslich, G.; White, T. J.; Cheetham, A. K. Mechanical Properties of Organic–Inorganic Halide Perovskites, $\text{CH}_3\text{NH}_3\text{PbX}_3$ (X = I, Br and Cl), by Nanoindentation. *J. Mater. Chem. A* **2015**, *3* (36). <https://doi.org/10.1039/C5TA03331D>.
- (96) Ma, L.; Li, W.; Yang, K.; Bi, J.; Feng, J.; Zhang, J.; Yan, Z.; Zhou, X.; Liu, C.; Ji, Y.; et al. A- or X-Site Mixture on Mechanical Properties of APbX_3 Perovskite Single Crystals. *APL Mater.* **2021**, *9* (4). <https://doi.org/10.1063/5.0015569>.
- (97) Giorgi, G.; Fujisawa, J.-I.; Segawa, H.; Yamashita, K. Cation Role in Structural and Electronic Properties of 3D Organic– Inorganic Halide Perovskites: A DFT Analysis. *J. Phys. Chem. C* **2014**, *118*, 41. <https://doi.org/10.1021/jp504479c>.
- (98) Zhu, H.; Cai, T.; Que, M.; Song, J.-P.; Rubenstein, B. M.; Wang, Z.; Chen,

- O. Pressure-Induced Phase Transformation and Band-Gap Engineering of Formamidinium Lead Iodide Perovskite Nanocrystals. *J. Phys. Chem. Lett* **2018**, *9*, 42. <https://doi.org/10.1021/acs.jpcclett.8b01852>.
- (99) Ghaithan, H. M.; Alahmed, Z. A.; Qaid, S. M. H.; Hezam, M.; Aldwayyan, A. S. Density Functional Study of Cubic, Tetragonal, and Orthorhombic CsPbBr₃ Perovskite. *Cite This ACS Omega* **2020**, *5* (13), 7480. <https://doi.org/10.1021/acsomega.0c00197>.
- (100) Gupta, Y.; Rathore, S.; Singh, A.; Kumar, A. Mechanical Response of Butylamine Based Ruddlesden Popper Organic-Inorganic Lead Halide Perovskites. **2021**, arXiv:2106.04960
- (101) Reyes-Martinez, M. A.; Tan, P.; Kakekhani, A.; Banerjee, S.; Zhumekenov, A. A.; Peng, W.; Bakr, O. M.; Rappe, A. M.; Loo, Y.-L. Unraveling the Elastic Properties of (Quasi)Two-Dimensional Hybrid Perovskites: A Joint Experimental and Theoretical Study. *Cite This ACS Appl. Mater. Interfaces* **2020**, *12*. <https://doi.org/10.1021/acsami.0c02327>.
- (102) Zhang, W.; Ye, H.-Y.; Graf, R.; Spiess, H. W.; Yao, Y.-F.; Zhu, R.-Q.; Xiong, R.-G. Tunable and Switchable Dielectric Constant in an Amphidynamic Crystal. *J. Am. Chem. Soc* **2013**, *135*, 7. <https://doi.org/10.1021/ja3110335>.
- (103) Al-Qatatsheh, A.; Morsi, Y.; Zavabeti, A.; Zolfagharian, A.; Salim, N.; Kouzani, A. Z.; Mosadegh, B.; Gharaie, S.; Au, A. Z. K. Blood Pressure Sensors: Materials, Fabrication Methods, Performance Evaluations and Future Perspectives, *Sensors*, **2020**, *20* (16) <https://doi.org/10.3390/s20164484>.
- (104) Cho, S.; Kang, S.; Pandya, A.; Shanker, R.; Khan, Z.; Lee, Y.; Park, J.; Craig, S. L.; Ko, H. Large-Area Cross-Aligned Silver Nanowire Electrodes for Flexible, Transparent, and Force-Sensitive Mechanochromic Touch Screens. *ACS Nano* **2017**, *11*, 7. <https://doi.org/10.1021/acsnano.7b01714>.
- (105) Dang, Z.; Shamsi, J.; Palazon, F.; Imran, M.; Akkerman, Q. A.; Park, S.; Bertoni, G.; Prato, M.; Brescia, R.; Manna, L. In Situ Transmission Electron Microscopy Study of Electron Beam-Induced Transformations in Colloidal Cesium Lead Halide Perovskite Nanocrystals. *ACS Nano* **2017**, *11* (2). <https://doi.org/10.1021/acsnano.6b08324>.
- (106) Dang, Z.; Shamsi, J.; Akkerman, Q. A.; Imran, M.; Bertoni, G.; Brescia, R.; Manna, L. Low-Temperature Electron Beam-Induced Transformations of Cesium Lead Halide Perovskite Nanocrystals. *ACS Omega* **2017**, *2* (9). <https://doi.org/10.1021/acsomega.7b01009>.
- (107) Ryde, L. Application of EBSD to Analysis of Microstructures in Commercial Steels. *Mater. Sci. Technol.* **2006**, *22* (11). <https://doi.org/10.1179/174328406X130948>.
- (108) Kamaya, M.; da Fonseca, J. Q.; Li, L. M.; Preuss, M. Local Plastic Strain

- Measurement by EBSD. In *Advances in Experimental Mechanics V; Applied Mechanics and Materials*, **2007**, 7 (8). <https://doi.org/10.4028/www.scientific.net/AMM.7-8.173>.
- (109) Muscarella, L. A.; Hutter, E. M.; Sanchez, S.; Dieleman, C. D.; Savenije, T. J.; Hagfeldt, A.; Saliba, M.; Ehrler, B. Crystal Orientation and Grain Size: Do They Determine Optoelectronic Properties of MAPbI₃ Perovskite? *J. Phys. Chem. Lett.* **2019**, 10 (20). <https://doi.org/10.1021/acs.jpcllett.9b02757>.
- (110) Demers, H.; Poirier-Demers, N.; Couture, A. R.; Joly, D.; Guilmain, M.; de Jonge, N.; Drouin, D. Three-Dimensional Electron Microscopy Simulation with the CASINO Monte Carlo Software. *Scanning* **2011**, 33 (3). <https://doi.org/10.1002/sca.20262>.
- (111) Muscarella, L. A.; Hutter, E. M.; Sanchez, S.; Dieleman, C. D.; Savenije, T. J.; Hagfeldt, A.; Saliba, M.; Ehrler, B. Crystal Orientation and Grain Size: Do They Determine Optoelectronic Properties of MAPbI₃ Perovskite? *J. Phys. Chem. Lett.* **2019**, 10 (20). <https://doi.org/10.1021/acs.jpcllett.9b02757>.
- (112) Levin, B. D. A. Direct Detectors and Their Applications in Electron Microscopy for Materials Science. *J. Phys. Mater.* **2021**, 4 (4). <https://doi.org/10.1088/2515-7639/AC0FF9>.
- (113) Sun, H.; Adhyaksa, G. W. P.; Garnett, E. C. The Application of Electron Backscatter Diffraction on Halide Perovskite Materials. *Adv. Energy Mater.* **2020**, 10 (26). <https://doi.org/10.1002/AENM.202000364>.
- (114) Kirchartz, T.; Márquez, J. A.; Stolterfoht, M.; Unold, T. Photoluminescence-Based Characterization of Halide Perovskites for Photovoltaics. *Adv. Energy Mater.* **2020**, 10 (26). <https://doi.org/10.1002/aenm.201904134>.
- (115) Futscher, M. H.; Gangishetty, M. K.; Congreve, D. N.; Ehrler, B. Quantifying Mobile Ions and Electronic Defects in Perovskite-Based Devices with Temperature-Dependent Capacitance Measurements: Frequency vs Time Domain. *J. Chem. Phys.* **2020**, 152 (4). <https://doi.org/10.1063/1.5132754>.
- (116) 3M™ Fluorinert™ Elektronikavloeistof FC-72 | 3M Nederland
- (117) Stolterfoht, M.; Corre, V. M. Le; Feuerstein, M.; Caprioglio, P.; Koster, L. J. A.; Neher, D. Voltage-Dependent Photoluminescence and How It Correlates with the Fill Factor and Open-Circuit Voltage in Perovskite Solar Cells. *ACS Energy Lett.* **2019**, 4 (12). <https://doi.org/10.1021/ACSENERGYLETT.9B02262>.
- (118) El-Hajje, G.; Momblona, C.; Gil-Escrig, L.; Ávila, J.; Guillemot, T.; Guillemoles, J.-F.; Sessolo, M.; Bolink, H. J.; Lombez, L. Quantification of Spatial Inhomogeneity in Perovskite Solar Cells by Hyperspectral Luminescence Imaging. *Energy Environ. Sci.* **2016**, 9 (7). <https://doi.org/10.1039/C6EE00462H>.

